Università degli Studi di Padova

Dipartimento di Ingegneria Industriale

Corso di Laurea Magistrale in Ingegneria Aerospaziale

Analysis and design of plasma thruster plume

Relatore: Ch.mo Prof. Daniele Pavarin

Correlatore: Dr. Marco Manente

Laureando: Andrea Grezzani

ANNO ACCADEMICO 2014-2015

To my Family
and all my Friends;
to all those people
who make Life a treasure.

Acknowledgements

Firstly, I wish to thank Professor Daniele Pavarin to be supervisor of this work.
A special thought goes to Dr. Marco Manente for his time, his constant help and support, and to the Ph.D. Fabio Trezzolani, who helped me with experiments and result comparison.
Least but never last, thanks to my family to always support me.

Abstract

The work investigates the effect of new components on the Helicon plasma thruster under development at CISAS (Center of Studies and Activities for Space, University of Padova) propulsion laboratory; then define a method to calculate a correction coefficient for Faraday cup that may be used to compute thrust. Eventually, a suggestion for improve for actual Faraday cup is given.

Contents

List of Figures

List of Tables

Chapter 1

Introduction

A compact low-power plasma thruster using high-efficiency radio frequency sources is currently under development by the European consortium HPH.com “Helicon plasma hydrazine combined micro” (7^{Th} Framework Programme of European Union). The main objective of the HPH.com research is to design, optimize and develop a spacecraft thruster based on radio frequency plasma source working in the Helicon range, and investigate on applications to mini-satellites for attitude and position control. The design of the thruster is pursued with a synergy of theoretical and experimental approach, also thanks to the development of highly innovative plasma codes. These codes are allowing for the first time a detailed and quantitative characterization of the Helicon physics involved in the RF coupling, and also on the physical mechanisms involved in the the plasma acceleration. [11–15]

This work investigates optimization possibilities for thruster currently under development at CISAS (Center of Studies and Activities for Space, University of Padova) propulsion laboratory and diagnostic used to evaluate its performances.
The aim of this thesis is to discuss:

- the effect of new components on the existing Helicon plasma thruster;
- the definition of a correction coefficient for a Faraday cup, with possible improvements, that may be used to compute thrust.

The dissertation is arranged in three chapters.
It starts with an introduction on plasma physics; then an overview on the thruster follows.
Second section deals with consequences due to new parts insertion on existing thruster; for every component effect on performances is evaluated and discussed with an electrostatic model. A review of PIC software is then treated as introduction for last geometry developed. Components evaluated include a capacitor in the outlet section, an external ground ring placed just after the diaphragm, two different cylinders internal to the chamber and an external ring at the same potential as one face the capacitor, positioned at different section of the physical expanding baffle.
Third and last part focuses on the analysis of effect of a Faraday cup. A correction coefficient is needed to compute thrust from ion current measurements; ion convergence on probe's front plate caused by its negative potential must be considered. An initial model is discussed for the configuration currently used in laboratory. An improvement is then presented and

investigated with different approaches. Correction coefficients for focusing effect of ions are finally found for Faraday cups in all cases.
Investigations are done with different numerical instruments, such as FEM and PIC software.

This work is entirely developed at CISAS.

Chapter 2

Background and overview

2.1 An introduction to plasma. Plasma Equations

Plasma is a gas made up of a large number of electrons and ionized atoms and molecules in addition to neutral particles as are present in a normal (non-ionized) gas. The most important distinction between a plasma and a normal gas is the fact that it presents a collective behavior: mutual Coulomb interactions between charged particles are important in the dynamics of a plasma and cannot be disregarded, so that an element of plasma exert a force on one another even at large distances.
Ionization in gases is usually produced as a result of collisions. When a neutral gas is in thermal equilibrium at temperature T, it has a certain degree of ionization, electrons being stripped off by collisions as a result of the thermal agitation of the particles. The numerical value is given approximately by Saha equation:

$$\frac{N_i}{N_n} = 2.4 \times 10^{21} \frac{T^{\frac{3}{2}}}{N_i} e^{\frac{U_i}{KT}} \tag{2.1}$$

where N_i and N_n are respectively ion and neutral densities (particles per m^3), K is the Boltzmann's constant and U_i the ionization energy of the gas. Ionization sources in gases will be treated lately.
When a gas is ionized, even to a rather small degree, its dynamical behavior is typically dominated by the electromagnetic forces acting on the free ions and electrons, and it begins to conduct electricity. The charged particles in such an ionized gas interact with electromagnetic fields, and the organized motions of these charge carriers can in turn produce electromagnetic fields.
Near the boundaries, typically metallic surfaces held at prescribed potentials or dielectric walls, strong space-charge fields exist in a transition region termed the plasma sheath. The sheath region has properties that differ from the plasma, since the motions of charged particles within the sheath are predominantly influenced by the potential of the boundary. The particles in the sheath form an electrical screen between the plasma and the boundary in a thin layer with dimension of few *Debye lengths*. In fact, when a *slowly* varying external electric field is applied to plasma charged particles start to move (electrons first, then ions) rearranging themselves and creating gradient regions on the walls, building up there an opposite field respect to the external one. This behaviour is exactly what we expect from a

conductor. Obviously, to properly screen external field an adequate high number of particles must be present. Anyway, the shielding is not complete because of thermal agitation. Potential of the order of KT/e can leak into the plasma and cause finite electric fields to exist there.
Another fundamental characteristic of plasma behavior is quasi neutrality, so that $N_i \approx N_e \approx N$ in the bulk; it follows from the property of conductors we have just seen: electric field inside them must be zero in *slowly* varying conditions. This is true in a macroscopic point of view; locally these quantity are not balanced, giving rise to interesting electromagnetic plasma effects (oscillations and waves).
For physics of plasma refer to [2, 4, 28, 30].

Maxwell's equations

We shall recall here electromagnetism equations.

Maxwell's equations in vacuum:

$$\nabla \cdot \vec{E} = \frac{\rho}{\epsilon_0} \tag{2.2}$$

$$\nabla \times \vec{E} = -\frac{\partial \vec{B}}{\partial t} \tag{2.3}$$

$$\nabla \cdot \vec{B} = 0 \tag{2.4}$$

$$\nabla \times \vec{B} = \mu_0 \left(\vec{J} + \epsilon_0 \frac{\partial \vec{E}}{\partial t} \right) \tag{2.5}$$

with obvious common notation.
Defining them using electric induction

$$\vec{D} = \epsilon_0 \vec{E} + \vec{P} = \epsilon_0 \epsilon_R \vec{E} \tag{2.6}$$

and magnetic induction

$$\vec{B} = \mu_0 \mu_R \vec{H} \tag{2.7}$$

to include in the definition the *bound* charge and current densities arising from polarization and magnetization of the medium, we can rewrite the equations above for dielectric materials as:

$$\nabla \cdot \vec{D} = \rho \tag{2.8}$$

$$\nabla \times \vec{E} = -\frac{\partial \vec{B}}{\partial t} \tag{2.9}$$

$$\nabla \cdot \vec{B} = 0 \tag{2.10}$$

$$\nabla \times \vec{H} = \frac{\partial \vec{D}}{\partial t} + \vec{J} \tag{2.11}$$

where ρ and $\vec{J}$ are now only the *free* charges and current.

Single particle model

For a charged particle moving in electric and magnetic field the equation of motion is:

$$m\vec{a} = q(\vec{E} + \vec{v} \times \vec{B}) \tag{2.12}$$

where the mass m of the particle should take into account relativistic effects. Clearly, the momentum of the single particle can be modified instantly by collisions with other particles. Using 2.12, Maxwell's equations together with the definition of current intensity

$$\vec{J} = \frac{1}{V} \iiint_V q\vec{v} dV \tag{2.13}$$

and current

$$I = \iint_S \vec{J} \cdot \vec{n} dS \tag{2.14}$$

the problem can be resolved.
In real systems number of particles are usually prohibitive to compute each single particle behaviour. Instead, PIC (Particle In Cell) algorithm are used: many similar particles are grouped together and moved every computational step, while fields are computed on a mesh. More information about PIC software will be given below.

Kinetic theory

Treating more particles together, one may describe a point in plasma using phase space distribution. We define distribution function as

$$f = f(\vec{x}, \vec{v}, t) \tag{2.15}$$

where

$$f = f(\vec{x}, \vec{v}, t) d\vec{v} \tag{2.16}$$

represent particles at point $\vec{x}$ with speed in the range $[\vec{v}, \vec{v} + d\vec{v}]$. Density in a point is then

$$n(\vec{x}, t) = \int_{-\infty}^{+\infty} f(\vec{x}, \vec{v}, t) d\vec{v} \tag{2.17}$$

Evolution of $f = f(\vec{x}, \vec{v}, t)$ is described by Boltzmann equation

$$\frac{\partial f}{\partial t} + \vec{v} \cdot \nabla f + \vec{a} \cdot \frac{\partial f}{\partial \vec{v}} = \left(\frac{\partial t}{\partial t}\right)_c \tag{2.18}$$

where last term is due to collisions, and with the assumption that *acceleration in one direction does not depend on velocity in that direction*. This is verified when Lorentz force is involved. When collision may be neglected, one obtains Vlasov equation

$$\frac{\partial f}{\partial t} + \vec{v} \cdot \nabla f + \vec{a} \cdot \frac{\partial f}{\partial \vec{v}} = 0 \tag{2.19}$$

Taking moments of these equations, one can obtain fluid model.

Fluid model

Considering plasma as made of only two different charged species, and taking averaged quantities over the velocity distribution (without any assumption of the *kind* of distribution) we obtain the complete series of two-fluids model equations reported here. It can be easily seen how fluid equations degenerate to particle equations when there are no pressure gradient and collisions. In this case average motion coincides with particle motion, being velocity differences and mutual interaction neglected.
Continuity equations:

$$\frac{\partial N_e}{\partial t} + \nabla \cdot (N_e \vec{u}_e) = 0 \tag{2.20}$$

$$\frac{\delta N_i}{\partial t} + \nabla \cdot (N_i \vec{u}_i) = 0 \tag{2.21}$$

with N particle density and $\vec{u}$ mean drift velocity.

Momentum equation:

$$m_e N_e \left[\frac{\partial \vec{u}_e}{\partial t} + (\vec{u}_e \cdot \nabla)\vec{u}_e \right] = -\nabla \cdot \vec{\vec{\psi}} + q_e N_e (\vec{E} + \vec{u}_e \times \vec{B}) + \vec{S}_e \tag{2.22}$$

$$m_i N_i \left[\frac{\partial \vec{u}_i}{\partial t} + (\vec{u}_i \cdot \nabla)\vec{u}_i \right] = -\nabla \cdot \vec{\vec{\psi}} + q_i N_i (\vec{E} + \vec{u}_i \times \vec{B}) + \vec{S}_i \tag{2.23}$$

where $\vec{S}$ is the momentum exchanged by collisions and $\vec{\vec{\psi}}$ is the pressure tensor. For cold plasmas, this quantity becomes negligible [1] .
Collisions model:

$$\vec{S}_e = v_{eff}(m_i N_i \vec{u}_i - m_e N_e \vec{u}_e) \tag{2.24}$$

$$\vec{S}_i = v_{eff}(m_e N_e \vec{u}_e - m_i N_i \vec{u}_i) \tag{2.25}$$

with v_{eff} accounting for the frequency of collisions.
Definition of current:

$$\vec{J} = q_e N_e \vec{u}_e + q_i N_i \vec{u}_i \tag{2.26}$$

The presence of neutral particles modify equations adding new collisions and source/sink terms.
Sometimes other linear combinations of these equations are used, known as MHD equations. They will not be discussed here. No hypotheses on distribution are made in *mathematical* derivation of also these equations; anyway, MHD fluid approach is valid whenever the distribution is maxwellian. Only many collisions can assure a *collective* drift of so different particles: only in this case the averaged quantities are then *physically* significative [30].

---

[1] Pressure tensor is defined as $\vec{\vec{\psi}} = mN < \vec{w}\vec{w} >$, with $\vec{w}$ thermal velocity due to temperature. An easy expression for this quantity can be found for isotropic problems. In particular for isothermal cases $P = NKT$.Anyway, for cold plasmas, the distribution is assumed to have zero averaged thermal velocity. For a more detailed discussion, useless here, refer to [30]

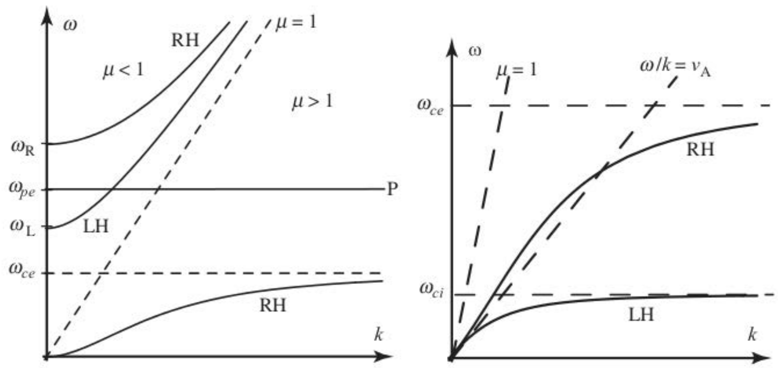

Figure 2.1: Dispersion diagram for waves in cold plasma. Effect of positive ions on wave propagation in a cold magnetoplasma: parallel propagation. The low-frequency end of the RH whistler mode is modified and a completely new LH ion-cyclotron wave branch appears. [30]

Plasma dielectric constant

We shall now define here the relative dielectric constant ϵ_R for collisionless cold plasma, for time-varying fields in presence of a constant magnetic field. We will consider first a frequency $\omega \gg \omega_i$ (ions motion can be neglected). This model is equivalent to assume infinite conducting plasma, with non-interacting electrons moving all together at average speed. Only inertia and magnetic force prevent electrons from perfectly shield external fields.
So on, we will obtain a formula for electric field that already includes current arising in plasma. By definition, similarly to what we have seen with dielectric materials, we have

$$\vec{\vec{\epsilon_R}} \cdot \vec{E} = \frac{\vec{J}}{jw\epsilon_0} + \vec{E} \tag{2.27}$$

where we continue to use two arrows to indicate 3×3 tensors. Using Maxwell's equations, momentum conservation for electrons and current definition (only *electronic* current) and assuming $\vec{z}$ direction pointing as $\vec{B}$ we obtain:

$$\vec{\vec{\epsilon_R}} = \begin{bmatrix} 1 - \frac{\omega_p^2}{\omega^2 - \omega_c^2} & -j\left(\frac{\omega_c}{\omega}\right)\frac{\omega_p^2}{\omega^2-\omega_c^2} & 0 \\ j\left(\frac{\omega_c}{\omega}\right)\frac{\omega_p^2}{\omega^2-\omega_c^2} & 1 - \frac{\omega_p^2}{\omega^2-\omega_c^2} & 0 \\ 0 & 0 & 1 - \frac{\omega_p^2}{\omega^2} \end{bmatrix} \tag{2.28}$$

where $\omega_c = \frac{q_e B}{m_e}$ is the cyclotron and $\omega_p = \sqrt{\frac{N_e q_e^2}{\epsilon_0 m_e}}$ plasma frequencies [2]. The value of $\vec{\vec{\epsilon_R}}$ in an arbitrary system of reference can be found using transformation with rotation matrices.

[2]For definition of such quantities [4, 28, 30]

When ions motion can not be neglected dielectric constant changes significantly. It can be shown [4] that in this case

$$\vec{\vec{\epsilon}}_R = \begin{bmatrix} S & -jD & 0 \\ jD & S & 0 \\ 0 & 0 & P \end{bmatrix} \tag{2.29}$$

where

$$\begin{aligned} R &\equiv 1 - \sum_s \tfrac{\omega_{ps}^2}{\omega^2} \left(\tfrac{\omega}{\omega \pm \omega_{cs}} \right) \\ L &\equiv 1 - \sum_s \tfrac{\omega_{ps}^2}{\omega^2} \left(\tfrac{\omega}{\omega \mp \omega_{cs}} \right) \\ S &= \tfrac{1}{2} (R + L) \\ D &= \tfrac{1}{2} (R - L)^* \\ P &= 1 - \sum_s \tfrac{\omega_{ps}^2}{\omega^2} \end{aligned}$$

with ω_{ps} and ω_{cs} s-species frequencies.

Expression for a general ϵ_R, with other species, collisions and temperature can be found in [30].

Sheath

Consider a plasma near a wall, in mono dimensional case. If ions are cold energy equation for one of them simply becomes

$$\frac{1}{2} m_i v_i^2(x) + e\phi(x) = \frac{1}{2} m_i v_{i,0}^2 \tag{2.30}$$

where $v_{i,0}$ is ion speed where $\phi = 0$, and we set this point to be $x = 0$. We'll use the subscript 0 for conditions at $\phi = 0$, used as a reference point. If we are considering steady-state conditions (no charge accumulation) continuity of ion flux imposes

$$n_i(x) = v_i(x) = n_{i,0} v_{i,0} \tag{2.31}$$

One then obtain for ions

$$n_i(x) = n_{i,0} \left(1 - \frac{2e\phi(x)}{m_i v_{i,0}^2} \right)^{-\frac{1}{2}} \tag{2.32}$$

Electrons can almost never be considered cold. Instead, their thermal velocity v_{th} is usually bigger than the drift velocity by some order of magnitude, so one can assume $v_{th} >> v_D$ (See Fig. 2.2).

Boltzmann equation then gives the steady-state density distribution for electrons - neglecting drift velocity

$$n_e(x) = n_{e,0} \exp \frac{e\phi(x)}{KT_e} \tag{2.33}$$

From Poisson equation

$$\nabla^2 \phi(x) = \frac{d^2\phi(x)}{dx^2} = \frac{e}{\epsilon_0} (n_e(x) - n_i(x)) \tag{2.34}$$

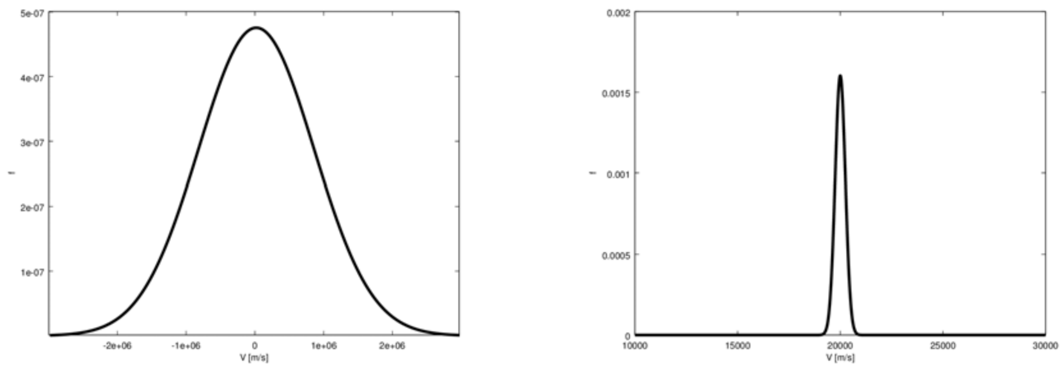

(a) (b)

Figure 2.2: Velocity distribution function for (a) electrons and (b) ions with a drift velocity of $v = 20000\frac{m}{s}$.

and using 2.32 and 2.33

$$\frac{d^2\phi(x)}{dx^2} = \frac{e}{\epsilon_0}\left[n_{e,0}\exp\frac{e\phi(x)}{KT_e} - n_{i,0}\left(1 - \frac{2e\phi(x)}{m_i v_{i,0}^2}\right)^{-\frac{1}{2}}\right] \tag{2.35}$$

If one consider the in reference point $\phi = 0$ quasi-neutrality occurs (zero point may be set arbitrarily), then $n_{i,0} \approx n_{e,0} \approx n_0$ and from 2.35

$$\frac{d^2\phi(x)}{dx^2} = \frac{en_0}{\epsilon_0}\left[\exp\frac{e\phi(x)}{KT_e} - \left(1 - \frac{2e\phi(x)}{m_i v_{i,0}^2}\right)^{-\frac{1}{2}}\right] \tag{2.36}$$

Multiplying left and right side of equation for $\frac{\phi(x)}{dx}$, integrating for x and imposing $\frac{d\phi}{dx} = 0$ for $x = 0$

$$\frac{1}{2}\left(\frac{d\phi(x)}{dx}\right)^2 = \frac{n_0}{\epsilon_0}\left[KT_e\exp\left(\frac{e\phi(x)}{KT_e}\right) - KT_e + m_i v_{i,0}^2\left(1 - \frac{2e\phi(x)}{m_i v_{i,0}^2}\right)^{\frac{1}{2}} - m_i v_{i,0}^2\right] \tag{2.37}$$

For a solution the right term must be not negative. At the entrance of the sheath $\phi(x) \to 0$ and one can expand in Taylor series. The non-negativeness requirement then becomes, neglecting third order and higher terms

$$\frac{1}{2}\frac{e\phi(x)^2}{KT_e} - \frac{1}{2}\frac{e\phi(x)^2}{m_i v_{i,0}^2} \geq 0 \tag{2.38}$$

for $x \to 0$, and then

$$v_{i,0} \geq \sqrt{\frac{KT_e}{m_i}} = v_B \tag{2.39}$$

This limit value is called *Bohm velocity* v_B, and the inequality is known as *Bohm sheath criterion*.

The differential equation can be resolved once boundary conditions are given.
For an isolated wall, at steady state, fluxes of ions and electrons balance. One can then find $\phi(x)$ curve declaring $\Gamma_i = \Gamma_e$ on the wall (noticing that flux for ions is all due to drift velocity while for electrons is due to thermal agitation) and an arbitrary value for plasma in plasma, say $\phi = 0$; the potential of wall is found to be

$$\phi_w = -\frac{KT_e}{e} ln\left(\frac{m_i}{2\pi m_e}\right) \tag{2.40}$$

If one wants to know potential drop between quiet plasma and wall simply uses

$$\frac{1}{2} m_i v_B^2 = e\phi_p \tag{2.41}$$

obtaining $\phi_p = \frac{KT_e}{2e}$, so

$$\phi_{pw} = -\frac{KT_e}{e}\left[1 + ln\left(\frac{m_i}{2\pi m_e}\right)\right] \tag{2.42}$$

Notice that for $v_i \to 0$ ions density $n_i \to \infty$; when drift velocity becomes so small, thermal velocity is no more negligible and model decade. Also $\frac{d\phi(0)}{dx} = 0$ is an approximation, because there is an electric field that accelerate ions to Bohm's velocity. Again, this is an approximate model.

For a wall with a fixed potential instead fluxes of particle can be not in equilibrium. In such a case, from equation 2.37 one can find electron and ion current reaching the wall.

Diffusion

Whenever there is a density gradient, plasma tends to diffuse toward regions of low density. A distinction should be suddenly pointed out: weakly ionized plasma diffusion behaves differently from fully ionized plasma. This is caused by the presence of neutrals that completely changes collisions mechanics. We shall discuss here fully ionized case only, because it's the condition we will use in this work. For weakly ionized diffusion and resistivity see [4].
Fluid equation of motion for electrons and ions are 2.22 and 2.23, repeated here

$$m_e N_e \left[\frac{\partial \vec{u}_e}{\partial t} + (\vec{u}_e \cdot \nabla)\vec{u}_e\right] = -\nabla \cdot \vec{\vec{\psi}} + q_e N_e(\vec{E} + \vec{u}_e \times \vec{B}) + \vec{S}_e \tag{2.43}$$

$$m_i N_i \left[\frac{\partial \vec{u}_i}{\partial t} + (\vec{u}_i \cdot \nabla)\vec{u}_i\right] = -\nabla \cdot \vec{\vec{\psi}} + q_i N_i(\vec{E} + \vec{u}_i \times \vec{B}) + \vec{S}_i \tag{2.44}$$

For highly ionized plasmas

$$\vec{S}_i = -\vec{S}_e = -\eta e^2 n^2 (\vec{u}_i - \vec{u}_e) \tag{2.45}$$

The value of η is given by Spitzer law

$$\eta = \frac{\pi e^2 m^{\frac{1}{2}}}{(KT_e)^{\frac{3}{2}}} ln\Lambda \tag{2.46}$$

with Λ maximum impact parameter

$$\Lambda = \overline{\lambda_D/r_0} \approx 10 \tag{2.47}$$

If electrons, being lighter, tend to leave plasma for thermal agitation or externally applied solicitations, a positive charge is left behind. Electric field set up by charge separation of such a polarity as to retard the loss of electrons and accelerate loss of ions. Eventually, both species will diffuse with same velocity. If $\vec{u}_i = \vec{u}_e$ then $\vec{S}_i = -\vec{S}_e = \vec{0}$.
Projecting equation of motion in $\vec{B}$ direction, at steady state, with small velocity space gradients

$$\begin{aligned} -eE_x + KT_e \tfrac{dN_e}{dx} = 0 \\ eE_x + KT_i \tfrac{dN_i}{dx} = 0 \end{aligned} \tag{2.48}$$

Electric field that build up has a "pushing" effect on ions, and decelerate electrons. Common mean drift velocity at equilibrium will be function of both electrons' and ions' velocities. If both species have zero initial drift velocity, then common mean ambipolar diffusion speed is Bohm velocity u_B; if they both have u_D drift initial speed, than at steady state they reaches $u = u_D + u_B$. Diffusion speed across $\vec{B}$ in fully ionized plasmas,using MHD equation, is found to be

$$u_\perp = \frac{\vec{E} \times \vec{B}}{B^2} - \frac{\eta_\perp}{B^2} \nabla p \tag{2.49}$$

with $\eta_\perp = 3.3\eta$. This diffusion does not involve any electric fields: the two species drift with same velocity from the start.
If, instead, one considers weakly ionized plasmas, flow dynamics is regulated by neutral-particles collisions. This results in a different speed of parallel diffusion and a completely different orthogonal diffusion coefficient. This last depends now on gyrating radius; diffusion is faster in ions than in electrons, so $\vec{v}_{\perp,i} > \vec{v}_{\perp,e}$ and an ambipolar electric field arise. Electrons thus have a "braking" effect on orthogonal diffusion.

2.2 Plasma sources: Helicon antennas

Helicon plasma sources are high efficiency, high density devices that creates a steady-state plasma from a gaseous propellant. Plasma production is sustained by absorption and propagation of Helicon waves, or bounded whistler waves, in magnetized plasma through the Landau damping mechanism. To launch the wave into the plasma, an axial magnetic field is applied in the ionization region and an RF antenna surrounding the plasma column couples to the plasma. The magnetic field direction and the antenna geometry determine the resultant wave propagation direction and wave pattern. The absence of electrodes in plasma prevents device failure due to the electrode erosion.
Helicon waves are electromagnetic waves that propagate in the frequency range $\omega_{LH} \ll \omega \ll \omega_{ec}$ in a finite space. Plasma current is assumed to be carried entirely by the drifting of electron gyration center, the frequency of Helicon waves being much less than the electron cyclotron frequency that electron gyration is too fast to matter, the wave frequency is much higher than the lower hybrid frequency so that ion motions do not contribute, and resistivity is zero. More, we're considering small amplitude waves, so equations can be linearized. We will therefore decompose the magnetic field in $\vec{B}_0 + \vec{B}$, the former being the constant part and the latter being the wave part. In Fig. 2.1, the Helicon branch is

represented by the lower curve on the left picture, and by the higher one on the left. We're looking for solution in a cylindrical domain, in the form $\vec{E} = \vec{E}(r)\exp(j(m\theta + kx + \omega t))$ and $\vec{B} = \vec{B}(r)\exp(j(m\theta + kz - \omega t))$.
From Maxwell's equations one obtains

$$\begin{aligned} -\nabla \times (\nabla \times \vec{E}) - \mu_0\epsilon_0 \tfrac{\partial^2 \vec{E}}{\partial t^2} = \mu_0 \tfrac{\partial \vec{J}}{\partial t} \\ \nabla^2 \vec{E} + \tfrac{1}{\epsilon_0}\nabla\rho - \mu_0\epsilon_0 \tfrac{\partial^2 \vec{E}}{\partial t^2} = \mu_0 \tfrac{\partial \vec{J}}{\partial t} \end{aligned} \tag{2.50}$$

and using definition in Eq. 2.27

$$\nabla^2 \vec{E} + \frac{1}{\epsilon_0}\nabla\rho = \mu_0\epsilon_0 \frac{\partial \vec{\vec{\epsilon}}_R \vec{E}}{\partial t} \tag{2.51}$$

For electromagnetic waves direction of propagation $\vec{k} \perp \vec{E}$; it follows that in Eq. 2.51 the terms $\frac{1}{\epsilon_0}\nabla\rho$ vanishes. Solution for Helicon waves is obtained solving

$$\nabla^2 \vec{E} = \mu_0\epsilon_0 \frac{\partial \vec{\vec{\epsilon}}_R \vec{E}}{\partial t} \tag{2.52}$$

or

$$\nabla^2 \vec{B} + \alpha^2 \vec{B} = 0 \tag{2.53}$$

in the domain of the antenna, with $\alpha = (\omega/k)[\omega_p^2/(\omega_c c^2)]$; for an isolating cylindrical boundary $(J_r)_{boundary} = 0$ and $(B_r)_{boundary} = 0$. Two mode solutions are represented in Fig. 2.3; general solutions for fields are given by linear combination of Bessel's functions

$$\begin{aligned} B_r &= A[(\alpha + k)]J_{m-1}(Tr) + (\alpha - k)J_{m+1}(Tr)]\cos(m\theta + kz - wt) \\ B_\theta &= -A[(\alpha + k)]J_{m-1}(Tr) - (\alpha - k)J_{m+1}(Tr)]\sin(m\theta + kz - wt) \\ B_z &= 2TAJ_m(Tr)\sin(m\theta + kz - wt) \\ E_r &= -A(\omega/k)[(\alpha + k)]J_{m-1}(Tr) - (\alpha - k)J_{m+1}(Tr)]\sin(m\theta + kz - wt) \\ E_\theta &= -A(\omega/k)[(\alpha + k)]J_{m-1}(Tr) + (\alpha - k)J_{m+1}(Tr)]\cos(m\theta + kz - wt) \\ E_z &= 0 \end{aligned} \tag{2.54}$$

with A wave amplitude.
The RF energy deposition per unit volume is calculated as the dot product of the current density and the electric field. However, only the axial component of the current and the electric field result in energy loss, as the transverse components of the electric field and the current are perpendicular to each other. Energy loss rate per unit volume can be computed as

$$-\frac{dW}{dt} = \vec{J} \cdot E = J_z B_z \tag{2.55}$$

and one finally finds [31]

$$\frac{dW}{dt} \propto |\alpha| B_z \tag{2.56}$$

Energy deposition is far more efficient than the one given by solving this equation, also if one consider Landau dumping and non-homogeneities. The phenomenon is still not completely clear. Antenna design must excite these oscillations. Some used geometries are reported in Fig. 2.4. For more on plasma antennas [5, 6, 23, 31].

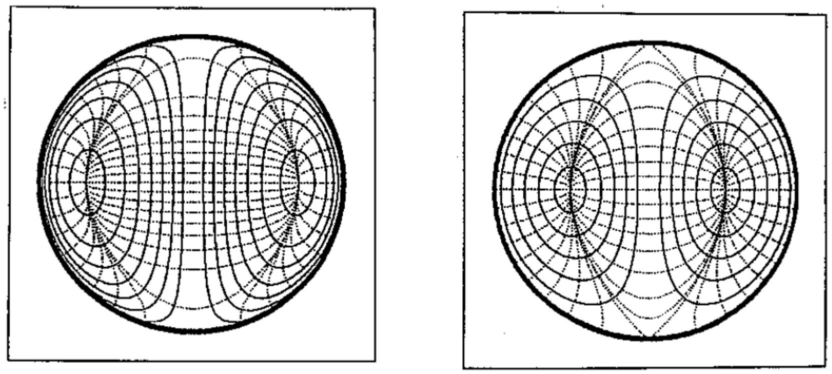

Figure 2.3: Pattern of magnetic (solid) and electric (dashed) field lines in the $m = +1$ and $m = -1$ modes of the Helicon wave in a uniform plasma in a plane perpendicular to the dc magnetic field [5].

2.3 Electric propulsion

Electric propulsion is a technology aimed at achieving thrust with high exhaust velocities, which results in a reduction in the amount of propellant required for a given space mission or application compared to other conventional propulsion methods. Reduced propellant mass can significantly decrease the launch mass of a spacecraft or satellite, leading to lower costs from the use of smaller launch vehicles to deliver a desired mass into a given orbit or to a deep-space target. In general, electric propulsion (EP) encompasses any propulsion technology in which electricity is used to increase the propellant exhaust velocity. Electric propulsion achieves high specific impulse by the acceleration of charged particles to high velocity. Different types of thrusters were invented during last decades for different range of applications; most famous are *resistojets, arcjets, ion thrusters, hall thrusters, magneto-plasmadynamic thrusters, VASIMR*. For space applications of plasma [1, 7, 10, 17].

A new and promising technology for space propulsion is the Helicon Plasma Thruster, a low-thrust high-I_{sp} propeller. The attractiveness of these devices is that in comparison with other electric propulsion devices, such as Hall thrusters, ion engines, MPDs, or arc-jets, this concept does not need any immersed electrode, grids or neutralizers. The lack of these components suggests that the HPT is a simple and robust device. A long lifetime is also expected, since the limited plasma-wall interaction due to the magnetic confinement reduces contamination or sputtering of sensitive components, e.g. the cathode in Ion or Hall thrusters.

2.4 The HPH.com project

The main objective of the HPH.com research is to design, optimize and develop a spacecraft thruster based on radio frequency plasma source working in the Helicon range and investigate on applications to mini-satellites for attitude and position control. We shall

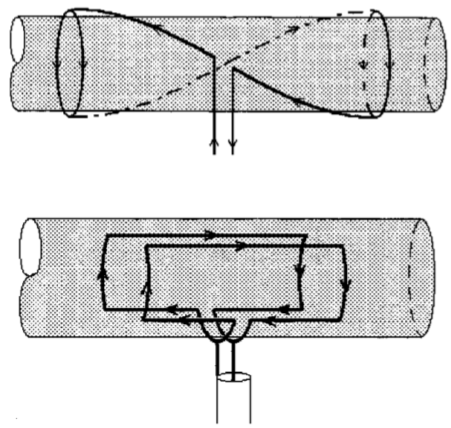

Figure 2.4: Example of Helicon antennas.

present here a review of principles on which the motor work. The thruster is a $50W - 1mN$ class, with a flow rate of $0.1 - 0.4\frac{mg}{s}$ and $I_{sp} > 1200s$; moreover, it can be used to heat and decompose a secondary propellant, in order to develop a second thrust mode. (with higher thrust but lower efficiency).

Additional and more detailed information can be found in [11–15].

The Helicon Plasma Thruster (HPT) is composed of the following parts (see Figures 2.5 and 2.6). A cylindrical chamber, where plasma is produced, typically slender and made of dielectric material (typically Pyrex glass) and a radio-frequency Helicon antenna wrapped around the chamber. The RF power is supplied to the antenna thanks to the RF subsystem, consisting on a power unit, a wave generator/amplifier, and a matching network, which adapts the RF power to the plasma electromagnetic behavior. A feeding system is commonly attached to the back of the chamber. Finally, a set of several electromagnets and/or permanent magnets surrounding the chamber generates the required magnetic field in both inside the chamber (mainly axial) and in the plasma expansion area, forming a divergent magnetic nozzle topology. Between the two, a convergent-divergent zone stops slow particles, making only the more energetic ones going outside. Regarding the HPT operation, different physical processes take place, involving among others: the emission and propagation of the wave from the antenna to the plasma; the absorption of the RF wave energy, which is deposited mainly on the electrons; these energized electrons bombard the neutral gas, producing a high density plasma; the generated plasma is confined and guided by the magnetic field; forward acceleration of ion is driven by the ambipolar electric field which naturally develops within the plasma to sustain quasi neutrality; along the magnetic field, plasma continues expanding supersonically. Thrust is understood as the increment of the momentum of the supersonic beam. The produced thrust is delivered to the thruster thanks to the interaction of plasma currents with the applied magnetic field. [17]

Unusual components are represented by the capacitor composed by the rings and the use of a diaphragm at the chamber exit, whose role will be discussed below; these are peculiar component of this particular project.

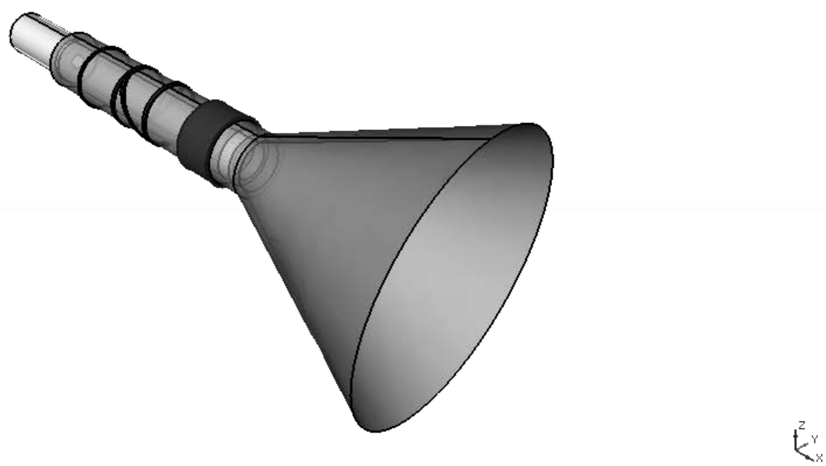

Figure 2.5: Schematic image of the motor without permanent magnets. The two rings at different voltage and the Helicon antenna are clearly visible.

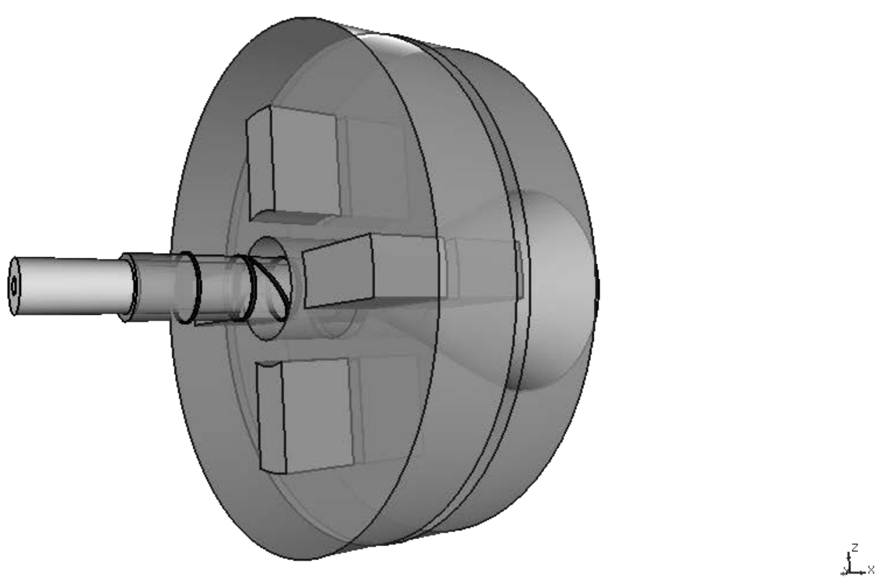

Figure 2.6: Schematic image of the motor with permanent magnets and inlet.

We will now take a look on how the thruster works.
During initialization Argon is injected in the cylinder from the inlet, and the correct neutral pressure is reached in the cylinder. Electric field created by the rings ionizes molecules of gas with intense voltage gradients over its dielectric rigidity; current raise in accordance to Townsend's discharge law and Paschen's curves. Once first charged particles are created, new plasma can be efficiently generated by Helicon antenna with a high ionization coefficient; electrons rapidly diffuse along the axis direction because of pressure gradient, constrained by magnetic field $\vec{B}$ and pushed by electric field $\vec{E}$. High inertia rate between ions and electrons makes the latter to only slightly move while former go far away; anyway, they finally start to move, pushed by electric field created from species density gradient and collision terms. A flow of charged particles starts to exit from the diaphragm, together with some unionized neutrals.

When fully working conditions are reached plasma inside the chamber assumes a positive (respect *space zero*) potential [3]. In the generation stage plasma tends, accordingly with its dielectric constant (Eq. 2.29) and local charge accumulations, to neutralize the external electric field leaving an almost iso-potential bulk. In the acceleration stage instead shielding is not complete, and there's no local quasi-neutrality indeed. Densities here are minor than in the production stage because of a sheath near the exit section, needed to equalize flux of different particles. The strong external electric field applied moves electrons, that rapidly rearrange themselves outside with effects on ions. An equilibrium state is eventually reached, with charges in the chamber that nearly shield the bulk from external fields in a thin sheath close to the walls, with a fluctuating density, and with a continuum flux of ionized particles with an average zero total net charge escaping the motor due to ambipolar diffusion from a thin hole with sound velocity.

Working conditions

The experiment works with Argon at an operational frequency of $f = 13.56MHz$ ($\omega = 8.5199 \times 10^7 Hz$). Plasma characteristics are reported in Tab. 2.1.

	Chamber	Plume
$N[m^-3]$	1×10^{19}	1×10^{15}
$T_e[K]$	46400	46400
$T_i[K]$	300	300
$\omega_{pe}[Hz]$	1.7837×10^{11}	1.7709×10^{9}
$\omega_{pi}[Hz]$	4.1481×10^{9}	4.1481×10^{9}
$\omega_{ce}[Hz]$	$\approx 2 \times 10^{10}$	≈ 0
$\omega_{ci}[Hz]$	$\approx 2 \times 10^{5}$	≈ 0
$\lambda_D[m]$	$4.7028 \times 10^{-6} m$	4.7016×10^{-4}

Table 2.1: Plasma parameters

[3] Positive potential is imposed by sheath on exit section and external dynamics of flow. See references [4, 16]

It's easy to verify that $\lambda_D \ll L$ in the chamber (L value may be found in Tab. 3.1) and $\omega > \omega_{ci}$, so ions' motion can be neglected when considering electrostatic field diffusion inside plasma. Values given in Tab. 2.1 are average parameters. Density changes substantially near the walls and in the exit region. The plume characteristics are taken at the ending section of the physical nozzle.

Chapter 3

Effect of new components on existing thruster model

In this section we shall speak about changes in electric and magnetic fields caused by insertion of new components or modification of existing parts. Accurate analysis of this aspect is fundamental for both starting instants, when the thruster is turned on, and for steady state, when it is fully working; moreover, we'll try to explain some behaviours found during tests and to see if these may really be related to changes in external field; then we'll try to find some guide-line for design a higher-thrust higher-I_{sp} motor.

Modelling the first ionizing field can be easily achieved. Neutral gas inside the chamber is isotropic and homogeneous. Evaluation of plasma behaviour instead is not a trivial task; to see why, we consider the acceleration stage of the motor. The presence of an Helicon antenna and a capacitor make fields varying both in module and direction. This makes dielectric constant of plasma being a populated time-varying tensor in the domain of interest.
Electric Field will be in the form

$$\vec{E}(\vec{x},t) = \vec{E}_1(\vec{x},t) + \vec{E}_2(\vec{x},t) + \vec{E}_3(\vec{x},t) \tag{3.1}$$

with $\vec{x} = (x, y, z)$, $\vec{E}_1$, $\vec{E}_2$ and $\vec{E}_3$ time-dependent components due to respectively the Helicon wave propagation, the voltage variation on the capacitor plates and the field due to charge distribution inside the plasma; far away from the Helicon source $\vec{E}_1 \to \vec{0}$ can be assumed.
In the same way, magnetic field will be

$$\vec{B}(\vec{x},t) = \vec{B}_0(\vec{x}) + \vec{B}_1(\vec{x},t) + \vec{B}_2(\vec{x},t) + \vec{B}_3(\vec{x},t) \tag{3.2}$$

with $\vec{B}_0$ the external static component imposed by magnets. We shall consider, in the acceleration stage, $\vec{B}_0 >> \vec{B}_1 + \vec{B}_2 + \vec{B}_3$, and then $\vec{B} \approx \vec{B}_0$.
Although the relation between fields is not linear, fields can always be represented as the sum of these components.
Some assumption will be made to let us investigate plasma behaviour only using vacuum calculated fields. Validation and a complete view of the physics involved is possible only

with PIC software.

Solution of electric field in the interest domain can be found using a FEM solver. For this purpose, we used the free software FEMM [24,26], a simple 2-D finite element pre- and post-processor, and solver. We took advantage, for a fast computation, of the axial symmetry of the system. For repetitive repositioning of components, we coupled OCTAVE scripting language with FEMM using the utility OCTAVEFEMM [25].

3.1 Effect on start

We have already said some words about the importance of starting instants model for electric field. It is in fact fundamental both in production of initial plasma, making antenna working only when really efficient (and coupled), and in acceleration of electrons to the outlet of the chamber in order to rapidly reach steady state and have an higher exhaust velocity. Electric field must be chosen in accordance to Paschen's law, that's in the figure presented below.

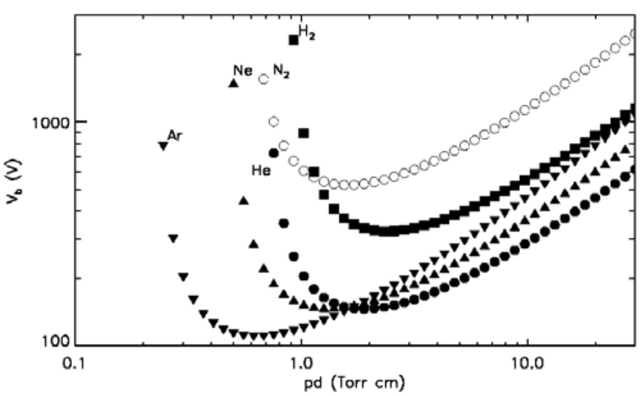

Figure 3.1: Paschen's curve for various gas. Argon is indicated with reversed triangles. Remember that $1Torr \approx 133.32Pa$, so $1Torr \cdot cm = 1.3332Pa \cdot m$.

Paschen's curve gives values for electric rigidity of gases; it represents voltage drop needed to create an electric discharge between two plates. Stable current from a dielectric raise when free electrons gain enough energy between successive collisions to ionise neutral atoms. The two free electrons then travel towards the anode and gain sufficient energy from the electric field to cause impact ionisation when the next collisions occur; and so on. This process is effectively a chain reaction of electron generation; it depends on the free electrons gaining sufficient energy between collisions to sustain the avalanche. Stable current state depends on number of particles (and then on pressure) because mean free path must allow electrons reach high enough kinetic energy before impact. Initial free electrons are those given from Saha relation, Eq. 2.1.

HPT developed at CISAS works with an initial neutral density is $P \approx 4Pa$; its value is regulated by fluid dynamics acting on the Macor ring internal diameter. Given an

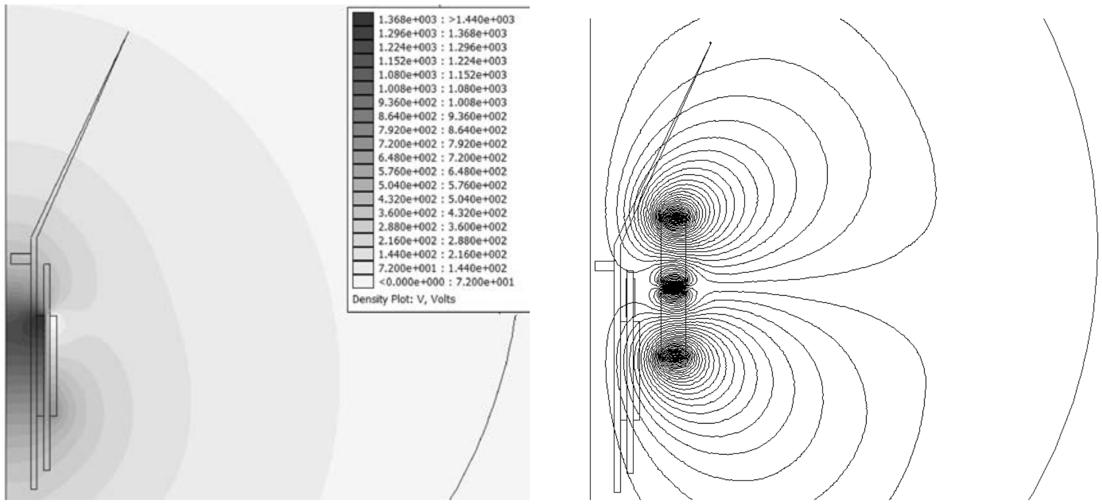

(a) (b)

Figure 3.2: Electrostatic potential in the chamber in starting case (a) and magnetic field lines (b).

approximate values for temperature of inlet flow of $300K$, we find from ideal gas law $P = N_n KT$ a density in the range $\approx N_n = 1 \times 10^{21}$. We assume a distance measured on axial line of force internal to the chamber around $70mm$ where we can see that almost all potential drop happens; then one obtains $P = 0.28Pa \cdot m$ and a minimum potential drop $\Delta V_{min} \approx 180V$ needed. The effective potential drop along the chamber axis is $\Delta V \approx 700V$, so requirements are largely satisfied. An image of potential is presented in Fig. 3.2. *Internal* field that one can see here may be considered unchanging for our purpose.

New components used during experiments do not modify so deeply *internal* electric field, so no influence they have on starting conditions. Ionization conditions are always satisfied. This will always be verified in all combination reported below.

3.2 Effect on acceleration stage

During experiments on the thruster a really strong modification of performance was observed due to insertion of new components in the motor. In particular, the repositioning of capacitor in the place shown in Fig. 2.5 led to a high improvement in performances. Contrary, the insertion of an internal cylinder made the system not working. We will now consider all experiences done and analyze effect on fields due to changing in configuration using a finite element software. For last geometry, a PIC model is developed.

As a reference for future comparison, we present in Fig. 3.2 electric potential due to the only Helicon antenna along the thruster in the instant when it is maximum. The electrostatic field may be considered zero in almost all the chamber when plasma is present. Due to high density in regions of $\nabla\phi$ charges accumulates near to the walls and shield the bulk in a really tiny layer on the order of some micrometers (see sheaths at 2.1).

3.2.1 Effect of the capacitor

As we introduced before, reposition of the capacitor in the vicinity of exit section shows an increment on performances of the thruster. Both thrust and I_{sp} grows up. More, the propeller starts to present a pulsating behaviour around an average equilibrium condition; density in chamber oscillates around the averaged value given for steady state without the capacitor. A physical insight on this phenomenon may lead us to formulate some suggestions to more improve the motor.
When the capacitor is inserted close to the antenna, electric potential field changes dramatically in the outlet region. Capacitor potential changes as a sine; one face is fixed at $0V$, the inner one can be described as

$$V(t) = V \sin(\omega t) \tag{3.3}$$

with $V = 1440V$.
Electric potential is calculated at instant $t = \frac{\pi}{2\omega}$. It oscillates around zero, assuming this values as maximum and the opposite as minimum. Calculated field is then a sample case representative of all behaviour.
A complete description of the FEM model is given for the first case, so it can be used as a reference for following ones.

Geometry

An initial geometry was present at CISAS. It was than modified to respond to experimental conditions: all parts were geometrically defined with their electric proprieties. Axial symmetry let us represent the problem in a 2-D environment. Due to simple geometry involved, everything was done using FEMM pre-processor utility. A 2-D model representative of the the motor with capacitor was finally obtained. Main dimensions and material proprieties are reported in Tab. 3.1; a figure of the final domain and geometry is instead reported in Fig. 3.3. All materials are considered isotropic.

$R_{main-cylinder}$	$9.5mm$
$L_{main-cylinder}$	$105mm$
$R_{max,baffle}$	$48mm$
$\epsilon_{R,Air}$	1
$\epsilon_{R,Pyrex}$	4.7
$\epsilon_{R,Macor}$	6
$\epsilon_{R,Quartz}$	5

Table 3.1: Geometry main dimensions and material proprieties.

Boundary conditions

Boundary condition for this open problem was $V = 0$ at infinite distance. An exact solution could be achieved by Kelvin transformation [26]; in our case a proper model was achieved by truncation of outer boundaries, so declaring $V = 0$ and $\frac{dV}{dn} = 0$ on a radius far enough from our system (to be influenced by it). This model was chosen for simplicity; no differences were seen using the aforementioned Kelvin application. Potential was then applied to lines inside the domain; Helicon antenna and capacitor had specified voltage, respectively $0V - 1440V$ linear drop along the antenna, $1440V$ on capacitor inner face and $0V$ on external one.

Mesh

Meshing was an important step in this first part. Only proper meshing gave us results good enough to be compared.
FEMM mesher utility creates an unstructured triangular-element mesh. Minimum allowable angle and size of elements may be set. A mesh influence analysis was started to know the right size to choose for convergence. To avoid too many elements, an inner region (with fine mesh) was defined inside a coarse mesh zone. To verify the optimum mesh size, an OCTAVE utility was written that compared results from two different meshes, one with half element size of the other; error was calculated as mean relative change at thousand sample points. A good mesh size was shown to be obtained setting $mesh - size = 1$; relative change in the solution using a mesh with half-size elements was $\approx 10^{-4}$. Mesh used is represented in Fig. 3.4.

Results

Results obtained are reported in Fig. 3.5 just for the acceleration stage.
A dramatic change in the exit section appears clearly. The analysis of the behavior leads to formulate some hypotheses about the involved physics; a description is reported below.

For a better understanding, we will analyze more deeply what happens when there is no capacitor. Particle that move to the exit must have a minimum velocity to escape the initially convergent magnetic field; the resultant distribution lacks the lowest velocities. In the outlet, sonic speed u_B [1] is reached. This is a consequence of charge conservation that must apply to motor chamber in steady state condition: outgoing charge flows must equilibrate. At the outlet, a sheath appears. This sheath can in first approximation be thought as a Bohm sheath. The value of potential ϕ on external section is determined by plasma dynamics outside the diaphragm; plasma potential ϕ_p inside the chamber adapts itself so in a way to equilibrate fluxes. Values of chamber walls ϕ_w can then be found using the Bohm sheath criterion. The divergent magnetic field $\vec{B}$ in the final part of the motor eventually accelerates the flowing particles to higher supersonic values.
We'll briefly see how external potential may vary motor behaviour.
When a strong external electric field is applied to plasma electrons rapidly move and reposition themselves in a way that shield the external applied electric force. Shielding *here* is far away from complete for two reasons: density is lower in the exiting region because of sheath formation and because flow shows a tendency to adapt its diameter to the diaphragm one, resulting in a plasma flowing region smaller than chamber dimension (see Fig. 3.6).

[1] Sound speed u_B should be calculated considering the presence of convergent magnetic field. The difference is not expected to be so high due to high difference between electron thermal speed and drift velocity.

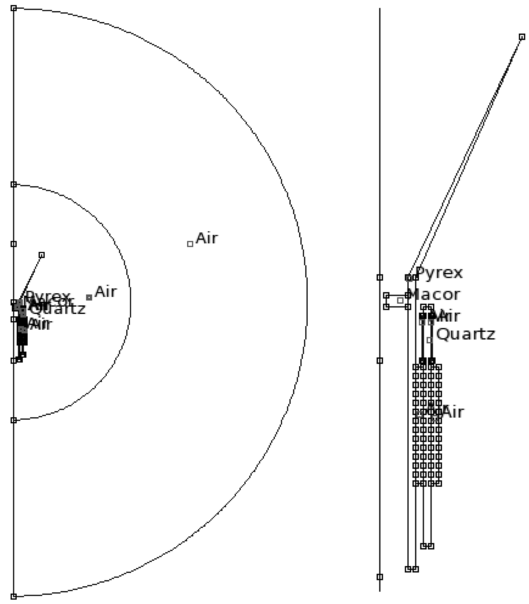

(a) (b)

Figure 3.3: Complete geometry with the capacitor. The large domain can be seen in left figure. In the right figure a zoom on the motor geometry is presented.

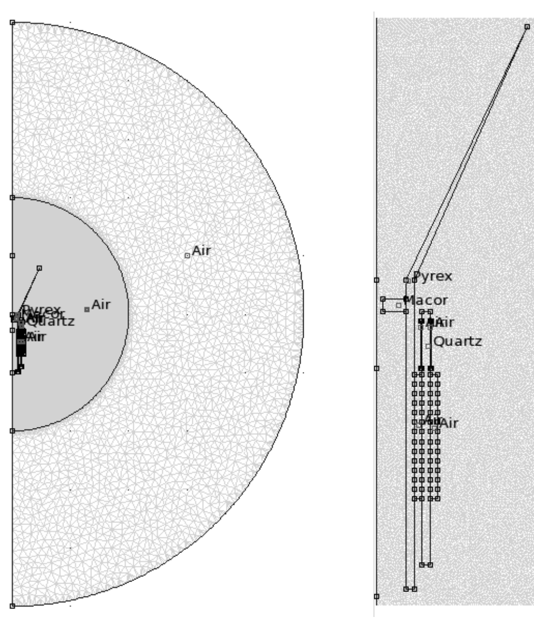

(a) (b)

Figure 3.4: Mesh in capacitor case. The large domain can be seen in left figure. In the right figure a zoom on the motor is presented.

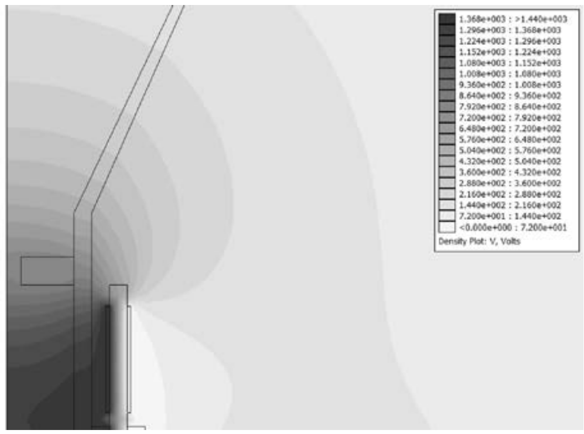

Figure 3.5: Solution in acceleration stage with capacitor.

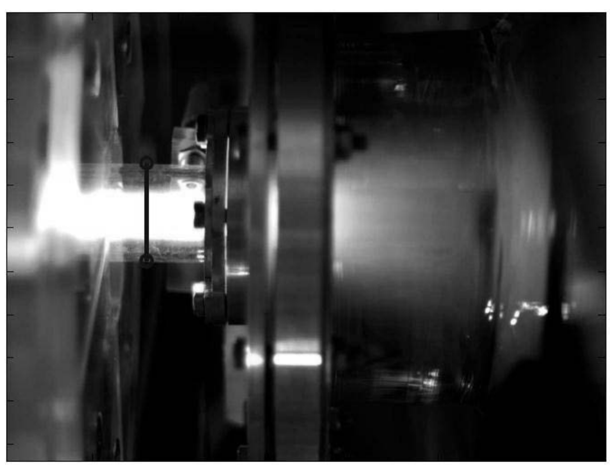

Figure 3.6: Plasma core diameter is smaller than geometry one.

Then a residual electric field $\vec{E}$ penetrates plasma in accordance with dielectric constant and local plasma accumulation.
An analytical solution can not be achieved. For now, we just let a residual electric field $\vec{E}$ being present in the plasma. For sure, this is a valid assumption for plasma in the outer radial position of the flow; in flow axis it should be proven. Anyway, a mean solicitations from external field is present on flow between two successive sections. We said that electrons are fairly more mobile than ions. This means that when $\vec{E}$ is pointing inside ($\vec{E}$ is almost axial) they will escape, leaving a net positive charged motor, and forming a negative cloud outside. Some ions are then accelerated and expelled for ambipolar effect.
When, instead, electric field is opposite directed electrons are slowed down; main part of them is trapped inside the chamber: they have no “pushing” effect on ions anymore. That would result in a distribution of velocities centered on lower value for ions and electrons; less particle than before can then escape magnetic convergent part. Flow, at this semi-period, will have lower velocities outside but, at the same time, lower mass flow.[2] Particles accelerated in the previous semi-period are of course decelerated; if electric field is concentrated in a really small region electron will be too far away to be recalled back. They don't really need to be *so* far away; they have just to reach a region with lower $|\vec{E}|$. Suppose ambipolar field to be really small respect to outer one, so $\vec{E} = \vec{E_3}$. With a simple calculation we can see how long electrons takes to escape electric field. Suppose that voltage decrease linearly in the outlet, so we can define a constant electric field. From Fig. 3.8 we can see that's fairly not true, but we'll assume it just to have an idea of order of magnitude. From basic law of motion

$$s - u_B t - \frac{1}{2} E_3 \frac{e}{m_e} t^2 = 0 \tag{3.4}$$

Assuming $E_3 \approx 10000 \frac{V}{m}$, $u_B = 3000 \frac{m}{s}$ and $s = 0.1m$, one can easily find escaping time $t \approx 1 \cdot 10^{-8} s$ for electrons, far less than oscillation period τ. An electric field 10 times less would be enough to complete escape. Even weaker field makes the same positive effect, without let the electrons to complete escape. Anyway, a strong field would influence more particles, enhancing the positive effect.
With same calculation one can see that ions need, with the same field, a time $t = 3\tau$ for a complete stop. In a semi-period they would loose less than $\approx 30\%$ of their velocity, and travel a distance $s < 1mm$.
Finally, averaging over a period, we find a positive increment on electron velocity, while ions velocity almost does not change. Because of the higher energy electrons have reached, velocity distribution will be higher and so the calculated diffusion coefficient (no substantial difference is in ions distribution of velocities). Ambipolar effect and charge accumulation translates distribution for exiting ions to higher value than normal (without electric field), resulting in a higher thrust and mass flow. See diffusion at 2.1.
Improvement in thrust may probably be connected to the better alignment of electric field and magnetic field too. A plot of β angle between the two for the exiting region is reported in Fig. 3.12. One can see that along the axis $\vec{E}$ and $\vec{B}$ are almost always parallel; electric field accelerates electrons, without creating useless azimuthal currents.

---

[2]Escaping velocity is fixed to Bohm value in the exit section. When electric field has a braking effect on a type of particle, they still flow with same velocity out of the throat. Loss of velocity (respect no $\vec{E}$ case) will be outside.

Analytical solution is not achievable. Electric field effect on flow depends on density and other plasma characteristics in the exit region; these depends on chamber conditions and external flow dynamics in the nozzle, than depends on electric field effect itself. Local charge accumulations must be evaluated. Additionally, the thruster due to the varying electric field has not a constant solution. The explanation given above must be intended as an interpretation of what may be the main factor.
Positive effect in thrust may also be due to the more collated plume.
A complete solution can be achieved only with numerical models using fluid approach or PIC software; with the latter, a complete view of the involved physics is possible, with information on the distribution of species.

3.2.2 Effect of a ground external ring

An external ring at $0V$ potential may be added in the external final part of the motor in addition to the capacitor, after the Macor diaphragm and just before the expanding baffle. This leads an increment of thrust and performances, enhancing the pulsating behaviour introduced before.

Geometry, boundary conditions and mesh

Geometry was slightly modified, adding the conductive ring. The ring is $5mm$ long and $0.5mm$ thick.
Boundary conditions remained the same as the case before; same voltage was also declared for capacitor and antenna. Only the condition $0V$ on the new ring was added.
The same mesh size as before was used. Convergence analysis showed that differences in geometry does not request any modification of the settings.

Results

Results are given in Fig. 3.7 for instant $t = \frac{\phi}{2\omega}$.
One can easily see that performances improve for the same reason we explained above. The ground ring enhances fast voltage drop, letting a strong electric field raise axially in a small region in the exit section. A comparison between V and E on the axis, with $x = 0$ on starting point of capacitor, for cases with and without the ring is presented in Fig. 3.8.
A so strong axial electric field varying in time can improve mean thrust and I_{sp}.

3.2.3 Effect of a internal cylinder

An internal cylinder was introduced inside the main cylinder during experimentation. This was an exploration to see how thickness of plasma flow combines with external electric field, applied as above. The motor showed an initial plume, than rapidly turned off. An instability was somehow reached. In this section the influence of fields with new geometry is discussed, and possibly related to the instability.

Geometry, boundary conditions and mesh

Macor diaphragm used had a slightly bigger hole than the previous one to permit insertion of the internal cylinder; its thickness reduced to $2mm$. The aforementioned cylinder was

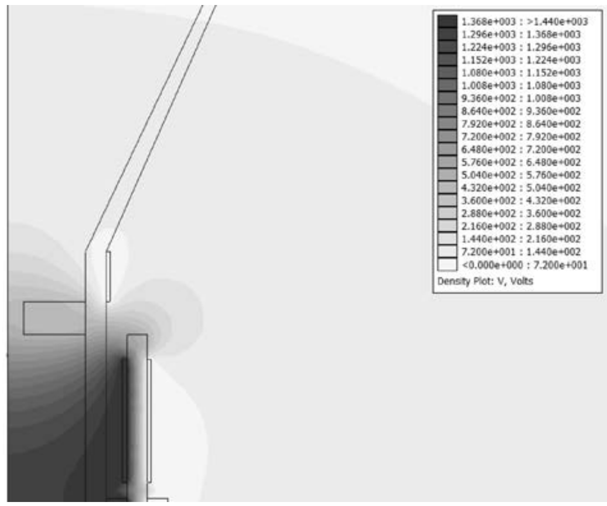

Figure 3.7: Electric potential in the case with ground ring at the exit.

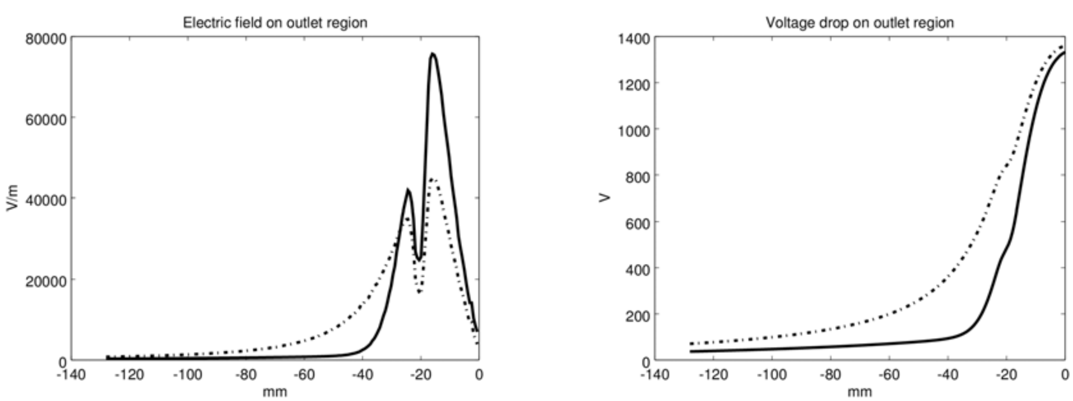

(a) (b)

Figure 3.8: A comparison of electric field (a) in axial direction and voltage drop (b) , in the axis. $x = 0$ is set on capacitor starting point. Dashed line is without ring; continuous line is with ring.

added. Then another similar geometry was tried, with a hollow cylinder. An OCTAVE script has been developed to test the influence of position respect to outlet section, starting form $5mm$ outside to $10mm$ inside with reference on the end of cylinder. Both geometries are reported in Fig. 3.9.

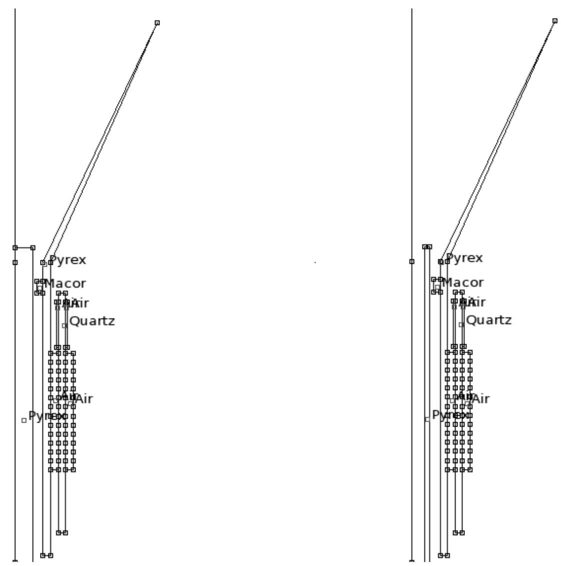

Figure 3.9: Geometries with internal cylinders, represented here in the outer position.

Boundary conditions are set to $V = 0$ at infinite (domain limits). Voltage was declared on internal conductors; same values as in previous cases are used for antenna and capacitor. Meshing was done with same settings as before.

Results

Results are in Fig. 3.10 for instant $t = \frac{\phi}{2\omega}$.
In Fig. 3.11 some reference values for V calculated for different position of the internal cylinder are given.
One can see that effect on field is visible and may change performances, but it should not be cause of instabilities. The cause of such behaviour during experiments may be connected to the different disposition of the flow. Without the central impediment, flow forms an axial flow (it does not even occupy all Pyrex tube, as is visible from Fig. 3.6). When the internal cylinder is inserted, plasma must flow at a radial distance R from the axis; also, dielectric constant of cylinder modify field lines in the outlet region. In this condition it passes a high $\vec{E} \times \vec{B}$ region, and a current starts to flow radially. Ions does not drift radially because they have a low gyration frequency; they exit almost undisturbed. Electrons instead give raise to the azimuthal current, drifting with a velocity

$$v_{E \times B} = \frac{\vec{E} \times \vec{B}}{B^2} \tag{3.5}$$

This uncontrolled current generated modifies local magnetic field, and may be the reason for instability. Fluid dynamics at the end of cylinder should also be studied, and may be

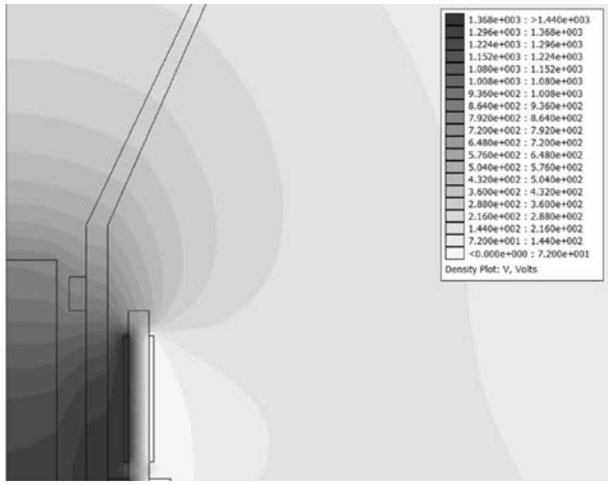

Figure 3.10: Solution in acceleration stage with capacitor and internal cylinder.

connected to instability too. A comparison between β angle between $\vec{E}$ and $\vec{E}$ with and without internal cylinder are reported in Fig. 3.12.

3.2.4 Effect of baffle dielectric constant

The influence of baffle dielectric constant is finally studied. The possibility of control $\vec{E}$ and $\vec{B}$ alignment accurately choosing the physic nozzle material is investigated. As we said before, this may lead to improvements on performances - keeping the two fields aligned - and to avoid instabilities.

Geometry, boundary conditions and mesh

Geometry was one used in the basic case, with capacitor. Baffle was divided from the Pyrex cylinder in order to declare for it an independent relative dielectric constant ϵ_R. The new material is taken to be isotropic.

Boundary conditions were set to $V = 0$ at infinite (domain limits). Voltage was declared on internal conductors.

The same mesh size as before was used.

Results

Results show that dielectric constant ϵ_R modifies beta angle, especially outside the baffle. Inside the cone the effect is not so determinant. Control of ϵ_R may be set to accomplish a best alignment between fields in order to achieve a better efficiency. A really high value of ϵ_R was used to enhance differences. This results should obviously be reviewed with all plasma dynamics inserted; anyway, it represents a good idea for future implementations.

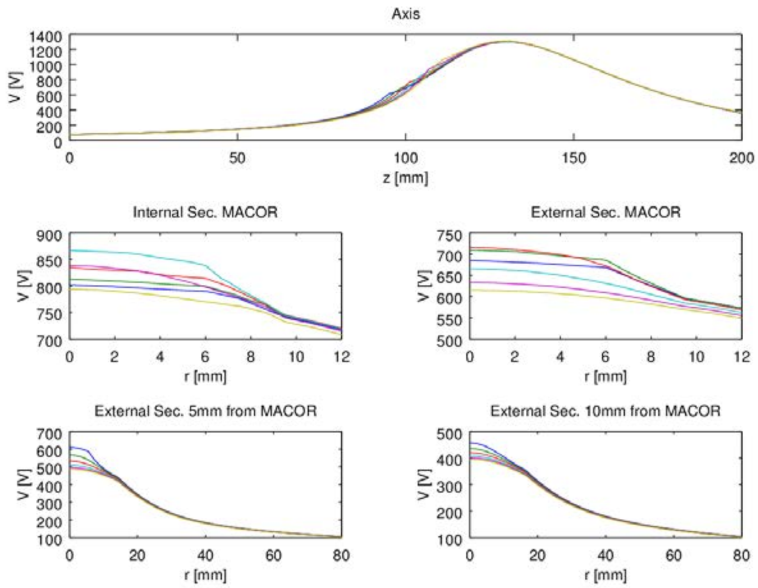

(a)

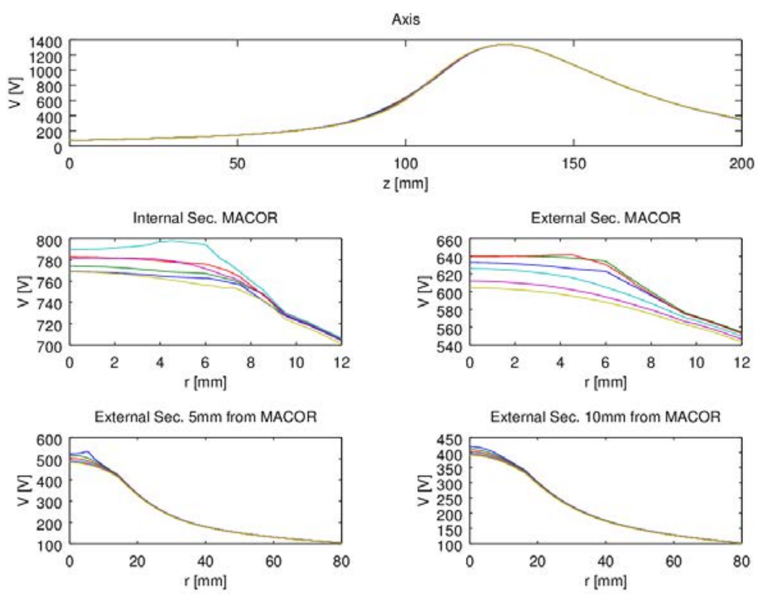

(b)

Figure 3.11: Voltage on some sections for different position of the internal (a) solid and (b) hollow cylinder, moving from external to internal. In axial graph, $x = 100$ is the outlet section.

(a) (b)

Figure 3.12: Beta angle with (a) and without (b) internal cylinder. Discontinuity of electric field on surface makes Macor ring and Pyrex walls visible.

3.3 Particle In Cell

Particle-In-Cell (PIC) is a method to resolve equation of motion of particle systems: individual super-particles are tracked continuously in a Lagrangian frame, whereas other quantities (such fields, densities and currents) are computed on Eulerian stationary mesh points. PIC method is relatively intuitive and straightforward to implement; it typically includes the following main steps:

- integration of the equations of motion;
- computation of possible collisions;
- interpolation of charge and current source terms to the field mesh;
- computation of the fields on mesh points;
- interpolation of the fields from the mesh to the particle locations.

The set of equations associated with PIC codes are therefore the Lorentz force as the equation of motion, solved in the so-called pusher or particle mover of the code, and Maxwell's equations determining the electric and magnetic fields, calculated in the (field) solver.

Particle clouds

In a PIC software, finite-size clouds are usually used instead of single real particles; these are often referred as *super-particle*. This gives two advantages: it reduces the number of particles to follow, and computational cost; it gives smoother solutions, giving a better representation of weakly coupled systems. Obviously, excessive particle accumulation may lead to wrong results. The effectiveness of this choice is connected to number of particles per unit of volume, and it's clearly valid when at high densities. For strongly coupled systems, where number of particle is low, single particle are followed. This last method is better known as Particle-Particle (PP). The mathematical formulation of the PIC method

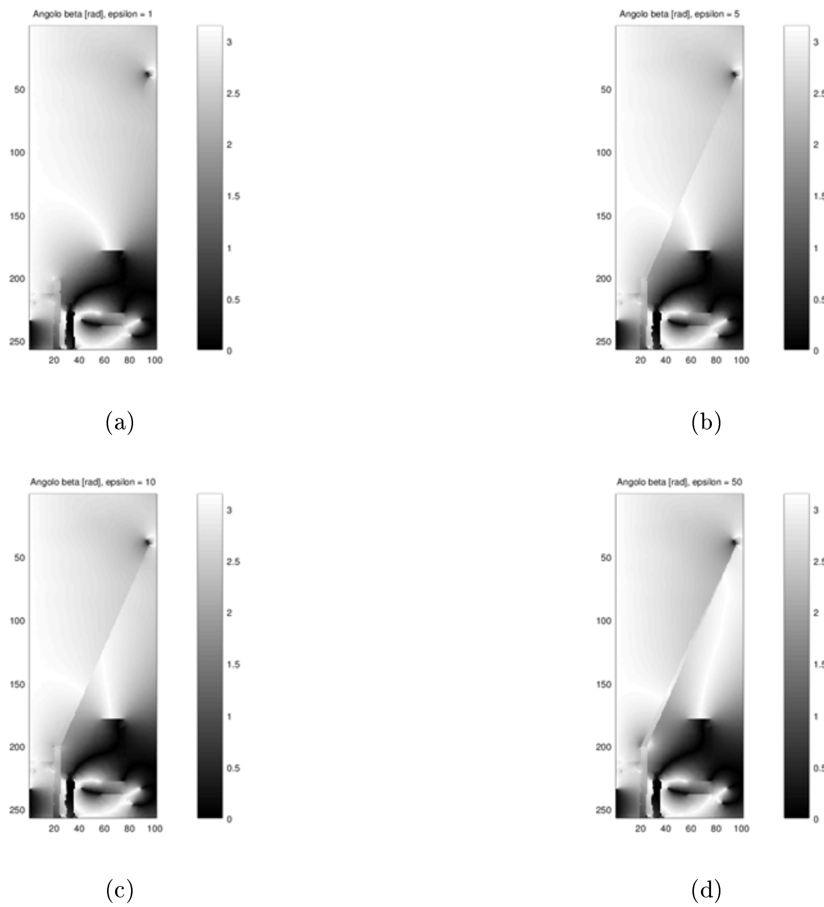

Figure 3.13: Beta angle with different ϵ_R for physical nozzle. Discontinuity of fields on surface makes Macor ring, Pyrex walls and magnets visible.

is obtained by assuming that the distribution function of each species is given by the superposition of several super-particle distributions:

$$f(\vec{x}, \vec{v}, t) = \sum_p f_p(\vec{x}, \vec{v}, t) \tag{3.6}$$

Clouds must be chosen to be physically significative and mathematically convenient: particle that are near each other in phase space are used. To each computational particle a specific functional form for its distribution is assigned; a functional form with a number of free parameters whose time evolution will determine the numerical solution of the Vlasov equation. The choice is usually made to have two free parameters in the functional shape for each spatial dimension, that have the physical meaning of position and velocity of the computational particle. For each particle distribution function will be

$$f_p(\vec{x}, \vec{v}, t) = N_p S_x(\vec{x} - \vec{x}_p(t)) S_v(\vec{v} - \vec{v}_p(t)) \tag{3.7}$$

where S_x and S_v are shape functions arbitrarily chosen. Proprieties of shape functions are:

- the support must be compact;
- their integral must be unitary;
- space symmetry should be respected.

Usually, S_x is taken to be a B-Spline while S_y a Dirac's Delta. The first choice is due to smoothing requirements, the second one by the physical need of keeping together particles and to calculate right force acting on each particle (Lorentz' force depends on $\vec{v}$).

Equation of motion

From moments of Vlasov equation for each super-particle distribution function one obtains

$$\begin{aligned} \frac{dN_p}{dt} &= 0 \\ \frac{d\vec{x}_p}{dt} &= \vec{v}_p \\ \frac{d\vec{v}_p}{dt} &= \frac{q_s}{m_s}(\vec{E}_p + \vec{v} \times \vec{B}_p) \end{aligned} \tag{3.8}$$

where $\vec{E}_p = \int S_x(\vec{x}-\vec{x}_p)\vec{E}(\vec{x})d\vec{x}$ and $\vec{B}_p = \int S_x(\vec{x}-\vec{x}_p)\vec{B}(\vec{x})d\vec{x}$ are the average fields acting on a super-particle. PIC method evolution equations above resemble the same Newton equation as followed by the regular physical particles. The key difference is that fields are computed as the average over the particles.

Field Solver

Field must be solved every step to obtain forces acting on super-particles. The solution of the field equations can be done with a wide variety of methods. The majority of the existing PIC methods relies on finite difference, finite volume or spectral methods. We shall focus on FEM methods.
Using FEM, the continuous domain is divided into a discrete mesh of elements. Charges and currents are calculated on mesh points using appropriate field weighting functions; sometimes they are approximated with a multipole expansion. Assignment must conserve total charge and current and be smooth. Most famous and used are NGP model (zero-order) and CIC model (first order); the second gives better results. A generic quantity Q (that may be scalar or not) is calculated at the i-th point as

$$Q_i(t) = Q(\vec{x}, t)W(\vec{x} - \vec{x}_i) \tag{3.9}$$

where $W(\vec{x} - \vec{x}_i)$ is the weight function.
When values at nodes are known, fields may be solved with usual FEM algorithms.

Particle mover

Even with particle clouds, the number of simulated particles is usually very large, and often the particle mover is the most time consuming part of PIC, since it has to be done for each particle separately. Thus, the integrator is required to be of high accuracy and speed. The schemes used for the particle mover can be split into two categories, implicit and explicit solvers. While implicit solvers calculate the particle velocity from the already updated fields, explicit solvers use only the old force from the previous time step, and are

therefore simpler and faster, but require a smaller time step. Some methods are Verlet, leapfrog, Boris and Vay schemes.
We'll briefly review leapfrog scheme here.
In leapfrog integration, the equations for updating position and velocity are, with reference to Eq. 3.8

$$\begin{aligned} \vec{x}_i &= \vec{x}_{i-1} + \vec{v}_{i-\frac{1}{2}}\Delta t \\ \vec{v}_{i+\frac{1}{2}} &= \vec{v}_{i-\frac{1}{2}} + \vec{a}_i\Delta t \\ \vec{a}_i &= \vec{F}_i \end{aligned} \tag{3.10}$$

where $\vec{x}_i$ is position at $i-th$ time step, $\vec{v}_{i+\frac{1}{2}}$ is speed at instant $i+\frac{1}{2}$. Position and velocity, with this method, are calculated at different instants. For plasma force $\vec{F}$ is Lorentz force, defined as in Eq. 3.8. The method it is stable for oscillatory motion, as long as the time-step Δt is constant, and $\Delta t \leq 2/\omega$. Initial velocity of the first time cycle must be moved by half a time step using an explicit method:

$$\vec{v}_{\frac{1}{2}} = \vec{v}_0 + \vec{a}_0\frac{\Delta t}{2} \tag{3.11}$$

Collisions

As considered till now, the method just considers Coulomb collision. In a real plasma, many other reactions may play a role, ranging from elastic collisions, such as collisions between charged and neutral particles, over inelastic collisions, such as electron-neutral ionization collision, to chemical reactions; each of them requiring separate treatment. Most of the collision models handling charged-neutral collisions use either the direct Monte-Carlo scheme, in which all particles carry information about their collision probability, or the null-collision scheme, which does not analyze all particles but uses the maximum collision probability for each charged species instead. With Monte-Carlo scheme, after particle motion is computed, probable collisions with target particles may be found. Every time the trajectory of a super-particle intersect a target particle, cross section is computed and then a random cycle is solved to establish if collision - and which kind of it - happened. Of course, kind of collisions possible are only those who are reachable on a energy point of view.
A representation of PIC model is given in Fig. 3.14
For more information on PIC [8, 18, 20, 21].

3.4 F3MPIC

F3MPIC is a PIC software entirely developed at CISAS for plasma studies.
Basic structure of the code follow guidelines given above.
The program manages 3D geometries while solving fields in 2D planes immersed in the plasma domain; with this approximation axisymmetric problems may be solved. Symmetry of fields is assumed around the axis, while no hypothesis are done on density distribution. A general symmetry is anyway expected on results.
By now the program implements an electrostatic model, with the magnetic field fixed solved by an external application (FEMM). Displacements currents are then neglected: in Eq. 3.8

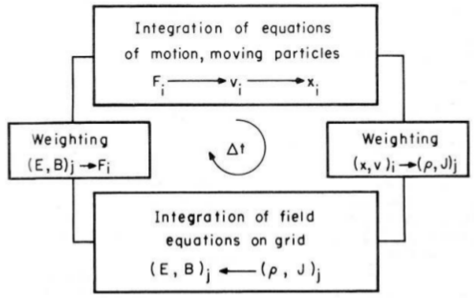

Figure 3.14: PIC scheme.

$B_p = B_0$ is assumed.
Multiple species may be simulated together, and particle number in super-particle may be set for each species.
The software uses GMSH [19] as standard for geometry definition and as meshing tool. Mesh is unstructured and made of tetrahedrons; its computation is based on Delauney-Voronoy algorithm. Fields are solved using FEM method. An external tool is used, namely GETDP [9] (standard FEM-solver that comes with GMSH); most post-processing is also based on GMSH, while some other output are just given as ASCII text files.
Particles are moved in 3D domain and motion may be integrated with leapfrog or Vay schemes. Collisions are computed with a Monte-Carlo method.
Using F3MPIC some attention is needed in order to obtain results. First of all, mesh size have to be smaller than Debye length in simulated conditions, so

$$L_{element} < \lambda_D \tag{3.12}$$

Moreover, time step must be chosen in order to satisfy Shannon theorem - using plasma oscillation period as reference frequency - and Courant-Friedrichs-Lewy stability criterion

$$\begin{cases} \Delta t \leq \frac{\pi}{\omega_p} \\ \Delta t \leq \frac{L_{elemento}}{v_p} \end{cases} \tag{3.13}$$

High densities require small elements and small time steps, leading to high computational times.

3.5 PIC simulation of geometry with external rings

Finally, in view of components optimisation, the influence of an external ring positioned on physical nozzle at same voltage as inner capacitor will be numerically investigated. This choice may seem in contrast with solutions seen in 3.2.1 and 3.2.2. An improvement in performances would be connected, now, not on highest velocity but on more aligned flux; it would lead, of course, on smoother voltage drops in outlet region, decreasing plasma mean exit speed.
Electric field produced by those external rings prevents electrons to escape due to thermal agitation, leading to a collimated flux of negative charges close to the axis that would in

turn give, as a consequence, a better alignment of positive charges. Ring position should be not too much away from exit region, to stop electron flow radius increase suddenly, but not too close to diaphragm for two reasons: not to modify too much situation discussed in 3.2.1, and to guarantee a adequate operative life to electrodes (a minimum distance of $2mm$ must be considered).
A complete set simulation with capacitor and external ring must be run to evaluate exact influence on performance, to see which situation gives best results.
Ring is moved in different positions and thrust is evaluated and compared in all cases.

A PIC model to evaluate performances was developed using F3MPIC. A description of the model and results will follow.

Geometry

Geometry was designed with respect to experimental conditions in GMSH environment. An initial model was already present at CISAS.
All elements already introduced are present in the model: chamber, diaphragm, physical nozzle and an expansion region outside. Electric elements are represented by antenna, capacitor and external rings.
More external rings were defined on the same geometry and the activated just one each simulation. This gave us the possibility of define just one geometry - and calculate mesh and covolumes only once - to use in different simulations, just varying BC.
Two different geometries were used to simulate more positions for rings.
External 3D domain boundary was kept enough far away from plasma developing region and from section of measure of thrust, in a way not to influence plasma in measure region; maximum dimensions of domain were dictate by computational time and memory requirements. Measure section was taken away enough far away from rings, so their action could be considered completed, and close enough to include all exiting ions, intercepting them before they reached lateral walls.
Planes for electric potential solution was choose to have boundaries enough far away from plasma domain, so BC defined on external radius may approximate infinity not disturbed value without modifying solution.
One of the geometries used is reported in Fig. 3.15.
Rings A, D and E are those visible in figure, respectively the first, second and third from diaphragm. Rings B and C are defined in another geometry between rings A and D.

Boundary conditions and super-particle sources

Boundary conditions are needed by PIC code to solve FEM problem. As boundary conditions, we should have specified only function value for undisturbed condition at infinity. The Dirichlet condition declared in the simulation was V = 0 at the line that in the model represents infinity.
Voltage value was declared also on antenna, capacitor and ring (a different ring every simulation) as a time varying function. The sinusoidal behaviour of potential was well represented in simulation due to small time step imposed by plasma, as we will discuss soon.

Walls outside chamber were modeled as dielectric, so particle impacting bounced on them. Recombinations at the walls are not currently modeled in F3MPIC. Inside chamber sheath condition was instead defined on walls: with this condition, electrons escaping form this surfaces are at each step compared to ions, and the difference is reinserted in tetrahedrals near the the wall. This imposition satisfies sheath that must form on boundaries for confined plasma, and let us obtain fast equilibrium conditions. A source rate was defined inside the chamber; rate of production was set to let the system reach desired densities at steady state.

Mesh

Tetrahedral mesh was build with GMSH. Size of elements must be smaller than Debye length in PIC simulation to see voltage fluctuation inside plasma. Dimension of elements was set to satisfy this condition; an approximate element dimension was found

$$V_{element} = \frac{V_{domain}}{N_{elements}} \tag{3.14}$$

and

$$V_{element} = \frac{L_{element}^3 \sqrt{2}}{12} \tag{3.15}$$

where tetrahedrons were taken to be, in first approximation, equilateral. Elements should not be taken too small to avoid memory occupation and too long computational times. Smaller elements were taken inside chamber and right outside, while larger elements where chosen in region of low density. As example, mesh for geometry in Fig. 3.15 is given in Fig. 3.16

Simulation parameters

Time step was limited by Eq. 3.13, by the need of represent in a good way electric field and by computational requirements. A final time step $t_{step} = 1 \cdot 10^{-9}s$ was selected. Simulation time selection was driven by steady state achievement. A first simulation was run to “fill” domain; a total time of $t_{simulation} = 9 \cdot 10^{-6}s$ was estimated from previous simulations. Then various cases were run for an enough long time $t_{simulation} = 5 \cdot 10^{-6}s$ to reach steady state with new boundary conditions, in order to correctly evaluate thrust and I_{sp}.

Particle clouds were made of 1000 charged particles for both species in plasma. Volume source creates $7 \cdot 10^{12}$ super-particles per second.

Results

Results were finally obtained and compared with experimental evidences present at CISAS from previous examinations. Data collected from simulations suggests that rings in physical baffle have a negative effect on performances, leading to lower average thrust and I_{sp} values than the original case.
Electron’s alignment - and then ions’ - is less convenient than a high electric field in convergent magnetic field zone in all simulated configurations.

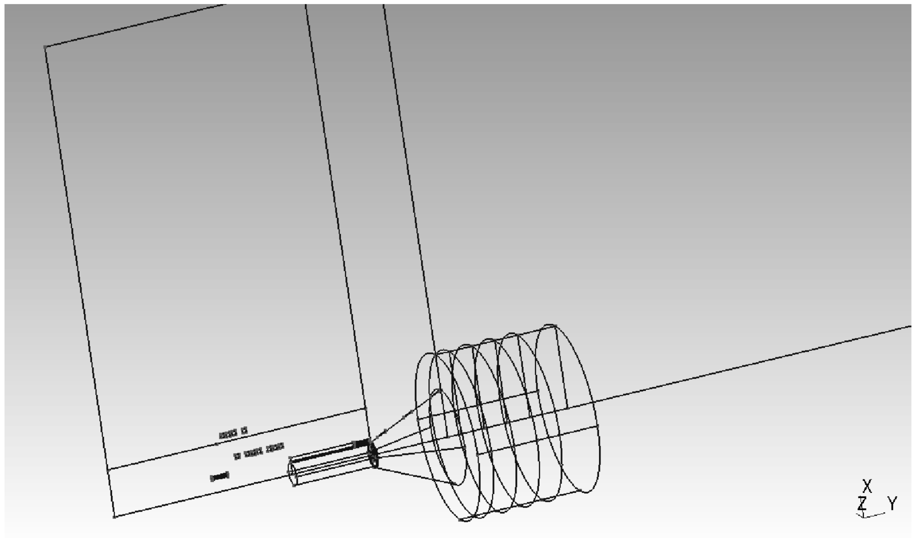

Figure 3.15: Geometry used in the simulation of the entire thruster with external rings.

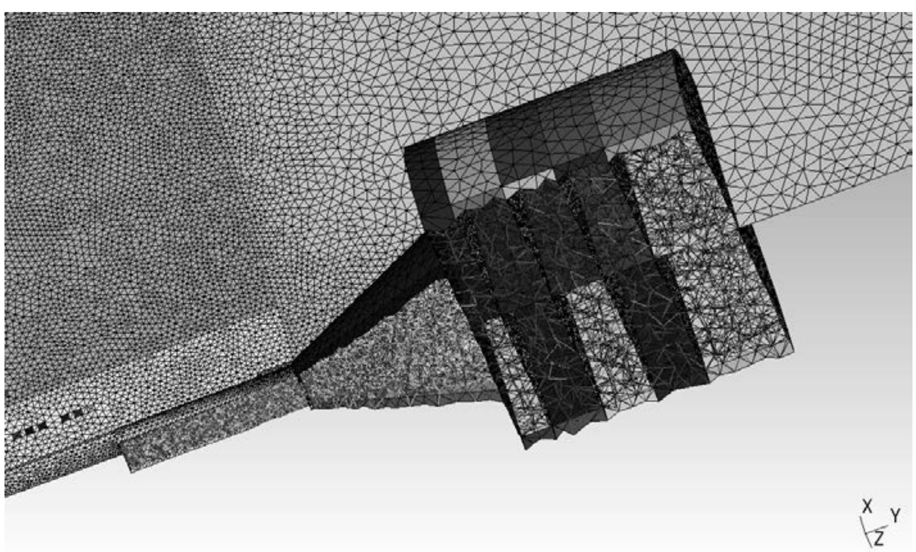

Figure 3.16: Mesh used in the simulation of the entire thruster with external rings.

Results of simulations for maximum thrust T_{max}, maximum specific impulse $I_{sp,max}$ together with total impulse calculated for a time of $t = 5 \cdot 10^{-6}s$ are given in Tab. 3.2. In the same table values of mean thrust T and I_{sp} are given, calculated from total impulse once average mass flow is known from simulations. This value was found to be $\dot{m} \approx 1.3 \cdot 10^{-12} \frac{kg}{s}$ in all simulations.

	T_{max} $[N]$	$I_{sp,max}$ $[s]$	I_{tot} $[Ns]$	T $[N]$	I_{sp} $[s]$
No external rings	$1.169 \cdot 10^{-7}$	$1.369 \cdot 10^{4}$	$1.580 \cdot 10^{-13}$	$3.160 \cdot 10^{-8}$	2478
External ring A	$1.056 \cdot 10^{-7}$	$1.499 \cdot 10^{4}$	$1.498 \cdot 10^{-13}$	$2.995 \cdot 10^{-8}$	2348
External ring B	$9.200 \cdot 10^{-8}$	9340	$1.463 \cdot 10^{-13}$	$2.926 \cdot 10^{-8}$	2294
External ring C	$6.902 \cdot 10^{-8}$	7490	$1.427 \cdot 10^{-13}$	$2.854 \cdot 10^{-8}$	2231
External ring D	$6.836 \cdot 10^{-8}$	6445	$1.475 \cdot 10^{-13}$	$2.951 \cdot 10^{-8}$	2314
External ring E **	$7.021 \cdot 10^{-8}$	7983	$1.191 \cdot 10^{-13}$	$2.382 \cdot 10^{-8}$	1868

Table 3.2: Complete thruster results. Total impulse is computed for $\Delta t = 5 \cdot 10^{-6}s$.

Worst performances are achieved with rings close to exit section. Ring D is enough far away to less influence acceleration region electric field, so performance start to increase again. Results for ring E are not comparable with others: potential drop generated is not completely developed at section of measurement for thrust. Those behaviours are in accordance with experimental results. From velocity distribution function on axis y for ions, one can see that best case is without external rings. Radial density and y velocity component distributions for ions and electrons for cases with no ring and ring A are showed at Fig. 3.17.

Just once, during experiments, performances showed an increment: that situation never repeated. A possible explanation for this fortunate case may be connected to finite delay of real electric components. For high operative frequencies wave length of signal may be compared with wire length, producing a phase shift between potential in different components. Probably phase shift was exactly that needed to let electrons feel first electric field, and then some focusing and pushing effect again in the second potential drop. Probability of having this situation is low because of all highly variable parameters involved.

Results seem to confirm real ones if scaled with density: mean velocity at Macor diaphragm is fixed by Bohm sheath criterion. Effect of electric fields should be re-evaluate with right density to keep into account for shielding accurately. Instant speed of electrons may differ from one obtained with simulations, and then real performances. If we impose in chamber a density $N = 1 * 10^{19}$ instead of $N \approx 1 * 10^{14}$ obtained with simulation, and assuming, with limitation we saw above, that thrust may be in first approximation scalable with density, one obtain a average value of $T = 3mN$ for base case in accordance with requirements and experimental results. Results found for external rings are then assumed to be valid for higher densities for the same reasons. Real performances differs from real ones due to neutral gas presence, that is not modeled.

Mean speed at outlet section is found to be one given by Bohm criterion, $v_B \approx 3 \cdot 10^3 \frac{m}{s}$, and then increase in the expanding magnetic field by a factor of 6.

Mass flow escaping the thruster (we said $\approx 1.3 \cdot 10^{-12} \frac{kg}{s}$) is far less than rate of source production, that, with simple calculations, results $4.6 \cdot 10^{-10} \frac{kg}{s}$. One should then notice

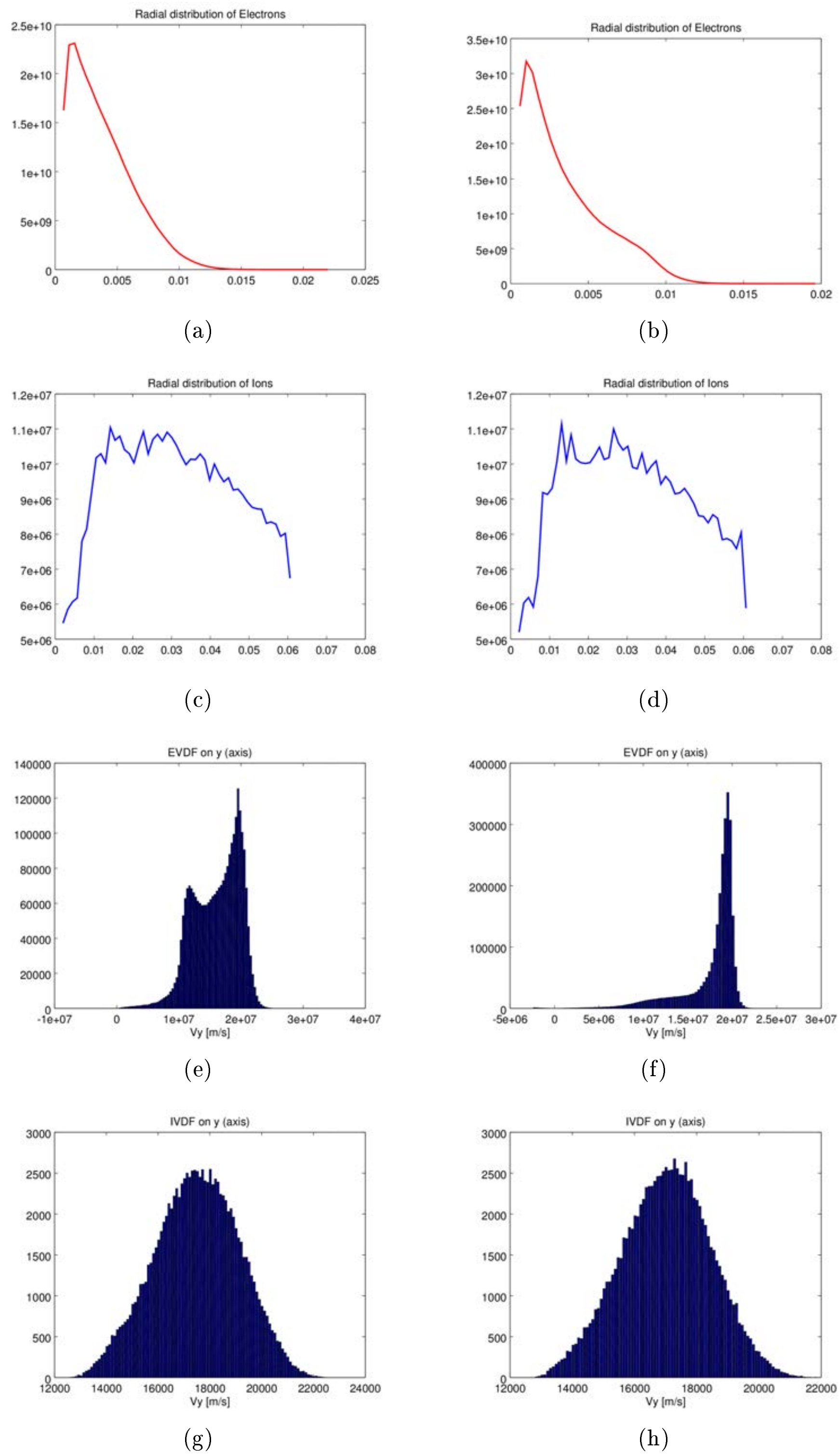

Figure 3.17: Electrons and Ions radial and velocity distribution in the y direction. Left column images (a-c-e-g) are those obtained without ring, right column (b-d-f-h) are results with external ring A.

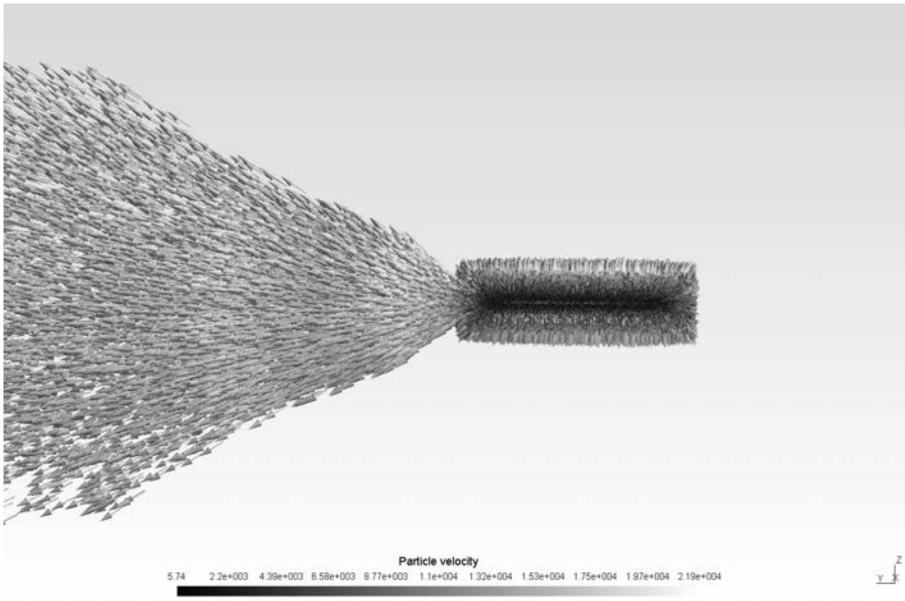

Figure 3.18: Solution for ions, obtained from PIC simulation.

that the two values represent, in real experiment, mass flow and rate of production of charged species in the antenna region. Argon inflow is in real condition almost equal to exiting plasma; two values differ for ion the thruster mass utilization efficiency η_m [7], which accounts for the ionized versus unionized propellant. Ionization rate is much bigger than escaping mass flow because re-ionization of particles that are neutralized at the walls must occur.
An interesting fact is that we do not see plasma cylinder radius adaptation at exit. Probably this lack is due to absence of neutrals; spectral analysis shows that neutrals tend to accumulate radially on final region of the thruster. Moreover, in the simulation source term is applied in all chamber region, while in real simulations it could be limited in certain zones.

Additional results will be reported in appendix .
The same model may be used to verify the effect of capacitor. This is also discussed in appendix.

Chapter 4

Faraday Probe correction coefficient

Thrust of a propeller is, from momentum equation,

$$\vec{T} = -\dot{m}\vec{v}_{outflow} \tag{4.1}$$

where $\dot{m}$ is mass flow and $\vec{v}_{outflow}$ the exhaust velocity at adapted pressure condition. For electric propulsion the simplification

$$\vec{T} = -\dot{m}\vec{v}_{outflow} \approx -\dot{m}_{ions}\vec{v}_{outflow} \tag{4.2}$$

holds due to high ratio $\frac{\dot{m}_{ions}}{\dot{m}_{electrons}}$.
Thrust may therefore be measured integrating ion current on all plume. Obviously only axial current gives rise to thrust: radial components, in a cylindrically symmetric system, cancel out. Ion current of the HPH.con thruster is sometimes measured with Faraday probe.

The Faraday probe (or Faraday cup) is a diagnostic tool used to measure ion current density of plasma. It could be used for electron current as well. While simple in principle and in implementation, in actuality, Faraday probe ion current measurements are extremely difficult to conduct accurately. There are several types of Faraday probes including nude, cupped, collimated, gridded, and a recent PEPL development, magnetically filtered probes. A standard Faraday probe (or nude probe) is biased below plasma potential to ensure that plasma electrons are repelled. Thus, a good estimate/measurement of electron temperature and plasma potential is essential to any good Faraday probe survey. The electric current of the FC is dependent on the incident particle beam current. In the case of ion beam or high energy electron beam detection, care must be taken because backscattered and secondary electrons may be ejected from the interior surface of the cup when the charged particles strike. These electrons may escape from the FC aperture. This results in the current overestimation for positive charged particle beams from the true values of current. To avoid this problem cylindrical FC designs have employed either coaxial electrostatic fields or magnetic fields to recapture the ejected electrons. Different designs were proposed to overcome this difficult [27]. Solutions are based on the use of an external guard ring, that recollect secondary electrons and let measurement corrections. With actual laboratory instrumentation, measurement of secondary current is not possible.
The non-zero potential on probe's front face makes boundary condition of our problem varying changing the field solution. We assume that this effect is only local and to not

Figure 4.1: Faraday cup with an electron-supressor plate in front.

modify motor behaviour; this assumption is experimentally confirmed. However, the focusing effect of particles must be considered and modeled, to see how much measured current on a surface S (corresponding to the instrument collector face) with the Faraday probe immersed in plasma differs from the real one that flows when there's no such probe in the flow. These two values may be highly different because of high energy of electrons in the tail of velocity distribution present in the plume. For right measurements, electrons should be completely repelled.
That means that really high negative potential on Faraday probe's front plate are needed, enhancing ion focusing.
If we assume a Maxwell distribution of velocity for incoming electrons, as represented in Fig. 2.2, one can see that $-10V$ on the front plate are enough to keep out the major number on negative particles; anyway, in laboratory measurements value down to $-150V$ are used.

In this section we shall analyze error in calculating thrust using the actual Faraday probe for current measurements. A first elementary electrostatic model (that only took in account potential generated from the probe's plate) that was used to calculate a reference index will be presented; results will be compared with experimental results. Then a solution to improve these kind of measurements will be introduced, and discussed with an electrostatic model. PIC simulation employed to refine results and experimental check will be finally described.
The purpose of this section is to identify an index to correlate undisturbed ion current to one measured in laboratory in the form

$$C_I = \frac{I_{measured}}{I_{ions,undisturbed}} \tag{4.3}$$

If really negative potential are used for Faraday probe, electron current may be neglected and

$$C_I = \frac{I_{measured}}{I_{ions,undisturbed}} \approx \frac{I_{ions,measured}}{I_{ions,undisturbed}} = C_{I,i} \tag{4.4}$$

We'll briefly review sheath problem in the simplest case to validate model; than we'll move on describing PIC model used and results. Computational requirements don't let us to use real experiment values for density N. For calculation, different values for N were chosen in order to extrapolate a good prevision for the case at hand.

For this purpose a F3MPIC PIC software was used.

4.1 Experimental conditions

Actual probe used for measurements consist in a negative biased plate insert, with a small indent, in a grounded guard cylinder. Current reaching the negative plate is measured with appropriate diagnostic. With actual diagnostic no other voltages may be applied to external ring, and no secondary electron current can be measured. Potential on the plate ranges in the $[0V, -150V]$. Actual FC is shown in Fig. 4.15 (a).

A fixed position for the probe will be considered, at $105mm$ from the outlet section along the axis. Plasma flow will be assumed to be undisturbed far away from the probe. Incoming flow present a radial component of speed; value for velocity is given from experimental measurements. Angle of divergence is measured in real conditions, and it has a value of $\alpha \approx 20°$. Plasma physical characteristic are those presented in Tab. 2.1 for plume. Ions are considered to be singly charged. Magnetic field will be neglected in all models. This is a strong assumption; anyway, we consider only a small portion of plasma along the axis. We therefore assume that here force lines are almost parallel to axis direction. Incoming plasma is considered completely ionized. A negative voltage is imposed in the inner plate of the probe; the remaining surfaces are all at ground potential. Dimensions of actual probe are presented in Tab. 4.1.

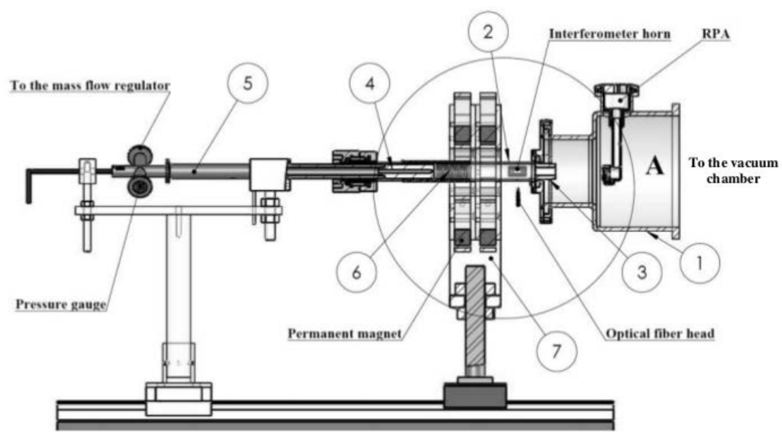

Figure 4.2: Overall CAD of the experiment and its main components: 1) Pyrex expansion bell; 2) Pyrex source (i.e. plasma source); 3) outlet diaphragm; 4) ceramic injector; 5) injection system; 6) antenna; 7) permanent magnets frame. Faraday probe may be inserted at the same position where RPA is.

Internal radius	$1.5mm$
External radius	$2.5mm$
Plate indent	$0.6mm$

Table 4.1: Actual Faraday probe's dimensions.

4.2 Electrostatic model for actual Faraday probe

Electrostatic model of Faraday probe aims to give an indicative correction coefficient for ion current measurement. If we suppose to set a negative enough voltage on probe's front plate ($-150V$), we may neglect electron current and assume Eq. 4.4 to hold. An electrostatic model may therefore used to calculate the focusing effect of ions assuming

$$C_I \approx C_{I,i} = \frac{I_{ions,measured}}{I_{ions,undisturbed}} = \frac{evN\pi r^2_{ions,measured}}{evN\pi r^2_{ions,undisturbed}} \tag{4.5}$$

where $r_{ions,measured}$ and $r_{ions,undisturbed}$ are ion flux tubes radius that finish into the front plate, measured far away from the probe (at infinity). If we use electrostatic model, ions are treated as single particles that approach probe with incoming drift velocity $v = 20000m/s$ and $n = 1 \cdot 10^{15}$ given by experiments.
As one can see from Eq. 4.5 density and incoming speed does not influence correction coefficient in this model. *Sheath effect and fluid-dynamics are not taken into account with the electrostatic model.* Moreover, divergence of fluid is not taken into account. This may be justified assuming that trajectory of ions are affected only close to the probe and close to the axis.
Undisturbed conditions should be taken at some Debye lengths from the probe; as we said, we're not considering sheath. So a far enough boundary is considered for undisturbed inflow to evaluate trajectory affecting distance in the worst case - without any electric screen.
All boundary is fixed at $0V$; plasma potential is neglected. Geometry - build using symmetry around axis - and mesh are developed within FEMM pre-processing environment.
Solution shows that voltage drop propagates in plasma region and expands radially. Electric field generates focus of ions on plate, increasing incoming ion current. An OCTAVE script was created to find $r_{ions,measured}$ in correction coefficient in Eq. 4.5 using field solution above, creating a particle at top boundary with starting velocity v and integrating its motion. Initial position of particle was increased radially starting from axial position and integrated in its motion. Maximum radius was found imposing as limit condition the collision with external ground circle of the Faraday probe.
Value of limit radius was found to be $r_{ions,measured} = 1.721mm$ with $V_{plate} = -150V$; trajectory for an Argon ion starting from position $x_{in} = (1.721, 80)$ is shown in Fig. 4.3.
Undisturbed ions are expected to flow straight, so $r_{ions,undisturbed} = 1.5mm$. Value of correction coefficient is found to be $C_I = 1.316$. Correction coefficient may be found in this way for each potential of the probe; anyway we would never account for shielding effect. Screening by plasma particles would modify correction coefficient for different densities, modifying electric field in domain. Values found with this model have to be treated as indicative.

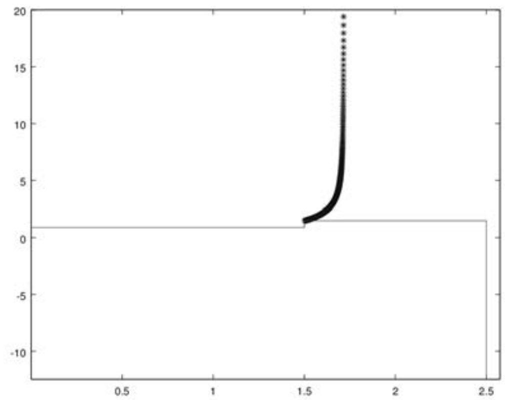

Figure 4.3: Last part of ion modified trajectory. Axis are not in scale. Half section of Faraday probe is visible in the bottom; symmetry axis is $x = 0$.

Deviation from original trajectory become sensible at distances $\approx 10mm$ from the probe, that at actual plume densities means $\approx 20\lambda_D$ (See Tab. 2.1). A voltage of $-150V$ is expected to be shielded by plasma in some Debye lengths, say $\approx 5\lambda_D$. Ion would be deviated later, and correction coefficient might differ substantially. A correct evaluation of C_I can be achieved with PIC, but simulations should be run for every potential of the plate and every density.

4.3 Faraday probe improvements

Improvements in the probe aims to avoid effect on measurements due to:

- front plate potential;
- density.

A solution to both these problem is found in increasing indent distance. This leads to benefits because potential drop is limited in a less extended area, with result that electric field is radially limited. Particle with starting radius $r > r_{probe}$ thus won't be focused on plate.
First approach for validation of the aforementioned solution was development exactly the same electrostatic model used for actual probe investigation, changing geometry. New geometry consist in a Faraday probe with dimensions presented in Tab 4.2.

Internal radius	$1.5mm$
External radius	$2.5mm$
Plate indent	$1.5mm$

Table 4.2: Improved Faraday probe's dimensions.

Trajectory of an Argon ion in this configuration with $V_{plate} = -150V$ may be seen in Fig. 4.4. Deviation from straight line is evidently reduced. Disturbed limit radius is $r_{ions,measured} = 1.554mm$; correction coefficient $C_I = 1.0733$.

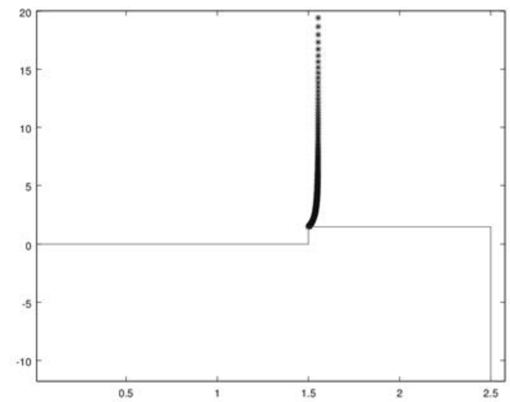

Figure 4.4: Last part of ion modified trajectory in improved case. Axis are not in scale. Half section of Faraday probe is visible in the; symmetry axis is $x = 0$.

The important point here is that thanks to this reduction, probe become almost insensible to plate potential. A voltage of $-10V$ would lead to a $r_{ions,measured} = 1.504mm$ and $C_I = 1.0053$; coefficient would change, in the worst case, of a 6.33%. The other point is insensibility from density. This can not directly be seen with this model. Anyway, one can understand that if potential drop is axial (and electric field does not propagate radially) screening distance does not influence results - electric field would, in the limit case of completely axial electric field, just accelerate ions towards the probe in axial direction. A comparison of electric potential in actual and improved case in front of the probe obtained with electrostatic model is presented in Fig. 4.5.

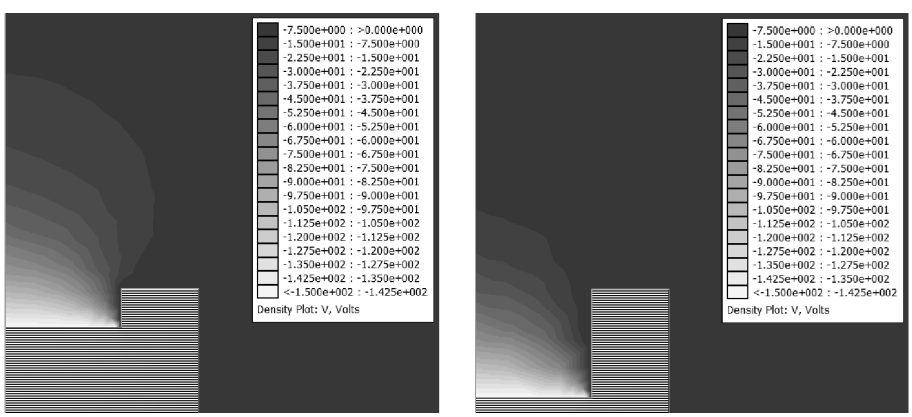

Figure 4.5: Field comparison in front of the probe, in actual and improved configurations.

4.4 PIC simulation of improved Faraday Probe

A PIC model of probe immersed in plasma is developed to calculate correction coefficients in Eq. 4.3 and Eq. 4.4 for the improved FC. A description of simulation of Faraday probe with F3MPIC will follow, focusing on all steps. Guide line of simulation are given below.

Values for current at different front plate voltage were measured for different densities, and compared with ones obtained in undisturbed conditions. A fixed position for the probe was chosen as described previously. Plasma flow was assumed to be undisturbed some Debye lengths away from the probe. Incoming flow present a radial component of speed; value for velocity was given from experimental measurements. Angle of divergence in real conditions ($\alpha \approx 20°$) would have request really large plasma domains (see 4.4) leading to long computational times. A smaller angle was then chosen. The flow develop entirely around the instrument also with this smaller value; result is not expected to change moving to the bigger real angle. Magnetic field was neglected. Also collisions and recombinations were neglected. Incoming plasma was considered as composed only by two singly caged species, electrons and Argon ions. Due to high rate ionization, no neutrals were considered.

Geometry

Geometry represents plasma domain around the Faraday probe.
Dimensions of the probe respected those in Tab. 4.2. As we said before, real flow divergence angle was too big, requesting high computational time. A smaller value was used: results obtained in this way are not expected to differ from bigger angle ones, because flow appears completely developed around the probe, and boundaries far enough from the probe zone of influence. So any bigger divergence angle would present same bulk conditions in zone influenced by the probe.
All flow should pass through the domain without touching walls, in order to adapt itself to vacuum conditions laterally. This is needed because when particles exit plasma domain, they're not more considered by the program and their influence on voltage is neglected. If particle exited domain before reaching the end of the domain, result would have been wrong. This requires lateral walls of the 3D domain to be enough far away from flow development region: one can see that bigger angle require bigger volumes, more elements and really high computational time. Emitter surfaces in F3MPIC insert particles in domain with a drift velocity perpendicular to them; thermal velocity is then automatically added to drift component. To emulate diverging field plasma emitter was represented by a spherical cap; its curvature radius was calculated to respect experimental conditions.
An emitter was positioned at several Debye lengths from probe's measure face. This was required to let flow develop completely in front of the probe and reach equilibrium, and then form sheath. As we'll see, inlet conditions were imposed for practical reasons without respecting the lateral sheath; flow needs some time - and some space - then to adapt. Exit section was defined some Debye lengths behind the probe. Due to difference in density, different geometry were used. Higher density means smaller Debye lengths, and from Eq. 3.12 smaller element. Smaller elements on same volume implies more tetrahedra. To obtain fast enough simulations, we used smaller 3D domains for higher density - lateral dimension only was scaled. This did not gave wrong results, because adaptation will occur radially in

smaller distances.

Plane for field solution were defined in all plasma domain, and outside. Radial dimension of the external region should be big enough to be considered infinite, letting us declare $V = 0$ on external line. Many Debye lengths are considered enough to achieve this result.

One of the geometries used is reported in Fig. 4.6.

In table Tab. 4.2 dimensions of Faraday probe are given; in Tab. 4.3 and Tab. 4.4 one can instead find respectively Debye lengths for simulated densities and dimensions of both geometries. As reference for probe dimensions see Fig. 4.1

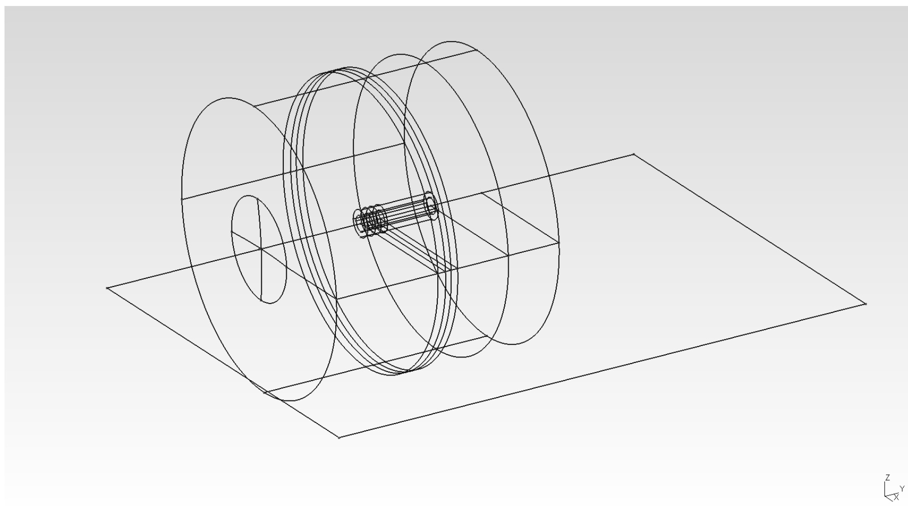

Figure 4.6: Geometry used in the simulation of the Faraday probe.

	$1 \cdot 10^{13} m^{-3}$	$1 \cdot 10^{14} m^{-3}$
Front distance from probe	$5cm$	$5cm$
Back distance from probe	$1cm$	$1cm$
Radius of emitter	$9.3mm$	$9.3mm$
Radius of 3D domain	$3.16cm$	$1.58cm$
Radius of 2D domain	$9.49cm$	$4.75cm$

Table 4.3: Geometry dimensions.

	$1 \cdot 10^{13} m^{-3}$	$1 \cdot 10^{14} m^{-3}$
Debye lengths	$4.7mm$	$1.5mm$

Table 4.4: Debye lengths.

Boundary conditions

Boundary conditions are needed by PIC code to solve FEM problem. As boundary conditions, we should have specified only function value for $r \to \infty$, as undisturbed condition. The Dirichlet condition declared in the simulation was $V = 0$ at the line that in the model represents infinity. Line was kept enough far away from domain to not influence solution. In cases where probe was present, $V = V_{plate}$ was declared on probe receptor while $V = 0$ was declared on all other instrument walls. Different simulations were run with V_{plate} assuming values in the range $[0V, -150V]$ with steps of $10V$.

Other conditions concern particle inflow. Particles are emitted from a surface and escape from all domain boundary. Inlet must emulate physical conditions and let the system reach the desired density around the probe. Keeping into account that almost all particles escape domain from the back surface, and that flow almost does not change diverging angle moving through the domain - total plasma flow is not modified moving around the probe - a first value of number of particles per second to insert may be found by

$$\Gamma_{particles,net} = NAv \tag{4.6}$$

with $A \approx A_{emitter}$, $v = 20000\frac{m}{s}$ and N desired density. This is *net flux* we expect on the emitter surface.

If we impose flux as in Eq. 4.6, with that drift velocity, this would result at steady state in a net flux $\Gamma_{net,particles}$ for ions but not for electrons. To see why, consider ions velocity distribution and electrons one given in Fig. 2.2. A part of the electrons that are inserted each step suddenly flows away from the emitter surface, resulting in a *net flux* minor than expected. Ions thermal speed instead is so low that probability of having particles flowing back is negligible. Thus, Eq. 4.6 holds well for ions but must be corrected for electrons. Assuming a Boltzmann distribution flowing in the domain, exiting flow to be balanced can be found averaging the distribution function over velocities in the negative axis direction. This must be done considering shifted distribution. Due to high thermal speed of ions respect to drift velocity, one can consider

$$\Gamma_{particles,electrons} \approx NA\frac{1}{4}\sqrt{\frac{8KT_e}{\pi m_e}} \tag{4.7}$$

with $\sqrt{\frac{8KT_e}{\pi m_e}}$ RMS average thermal velocity in a direction, in a 3D maxwellian distribution. Finally, Eq. 4.6 was used for ions in inlet conditions while Eq. 4.7 for electrons, modified in a way to account for super-particle accumulation.

When undisturbed case was simulated, so without probe in the domain, model used was the same in other cases but no electric condition, as we said, was given at probe surfaces. On all surfaces instead a condition was fixed so ions and electrons fluxes were compared each steps, and electrons in excess respect to ions - due to thermal motion, because quasi neutrality is expected - were reinserted in domain. This option was available in F3MPIC.

Mesh

Tetrahedral mesh was build automatically using GMSH tools, setting size of elements in regions of interest. A fine mesh was used in front of probe, while a coarse one was choose for the rest of domain. We remark here that size of elements must be smaller than Debye length, as we already mentioned, to see potential gradients inside plasma. Dimension of elements was set to satisfy this condition; and a final check was run using Eq. 3.14 and Eq. 3.15. Number of elements and typical length calculated with Eq. 3.15 is shown in Tab. 4.5 and may be compared with Debye lengths for same densities at Tab. 4.4 to see it respects Eq. 3.12.

	$1 \cdot 10^{13} m^{-3}$	$1 \cdot 10^{14} m^{-3}$
Number of elements	613929	422000
Element edge	$1.4751mm$	$1.0518mm$

Table 4.5: Mesh parameters in PIC simulations.

Mesh used in one of the cases in shown in Fig. 4.7.

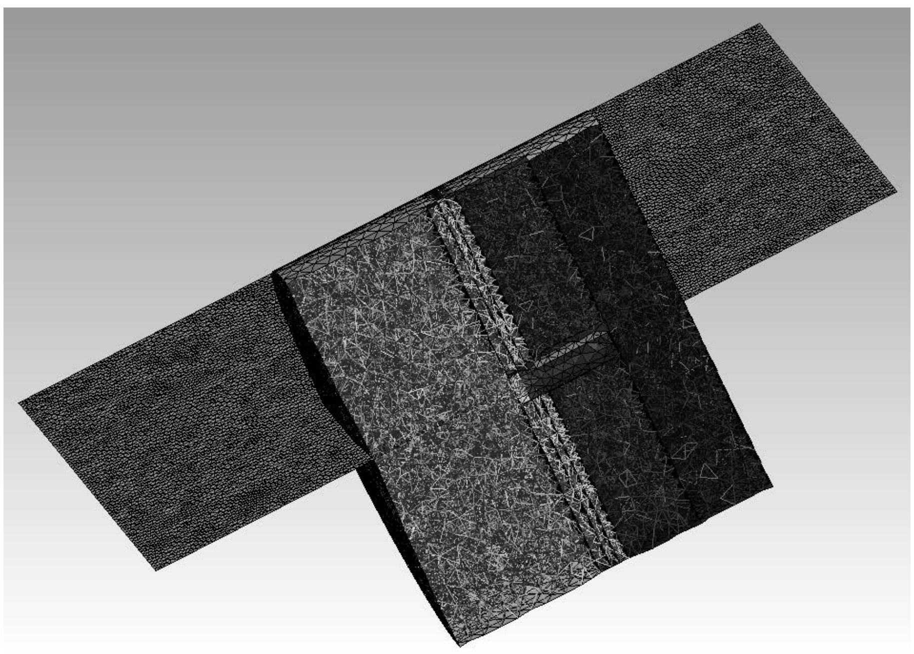

Figure 4.7: Geometry used in the simulation of the Faraday probe.

Simulation parameters

Time step and convergence time have been accurately choose to obtain good results.
Time step was chosen in accordance to Eq. 3.13, to Courant-Friedrichs-Lewy stability criterion and Shannon theorem. The most limiting requirement was given by high plasma frequency. Time step should not have been taken to small; this would have lead to long computational times. Final values used for different simulations are reported in Tab. 4.6 with plasma frequencies.

	$1 \cdot 10^{13} m^{-3}$	$1 \cdot 10^{14} m^{-3}$
Time step	$1 \cdot 10^{9}$	$5 \cdot 10^{9}$
Plasma Frequency	$2.84 \cdot 10^{7}$	$8.98 \cdot 10^{7}$

Table 4.6: Time step in PIC simulations.

Convergence time was calculated as time for particle to reach the exit section of the domain, in order to have a developed plasma and a stable number of particle. For this aim, a total time of simulation of $t_{simulation} = \frac{L_{domain}}{v} \approx 3.25 \cdot 10^{-6} s$ was approximately calculated. Monitoring number of particles in complete domain, a complete convergence was discover to happen for $t_{simulation} = 4 \cdot 10^{-6} s$. Total step in one simulation were almost 10^3.

For both species super-particles of 1000 elements were chosen.

Results

Results show what we expected. Main modification on ions current is due to presence of the probe itself, but now measurements are almost independent from bias voltage and density. Probe actually screen itself, and electric field does not propagate radially in plasma recalling ions. All voltage drop happens in front of the plate, in a really thick layer - some Debye lengths. One of results for potential field is reported in Fig. 4.8. Screening effect is visible - drop is limited in a minor region respect to same case simulated with electrostatic model, in Fig. 4.5. In Fig. 4.9 and Fig. 4.10 is possible to see developed flux, respectively for ions and electrons.

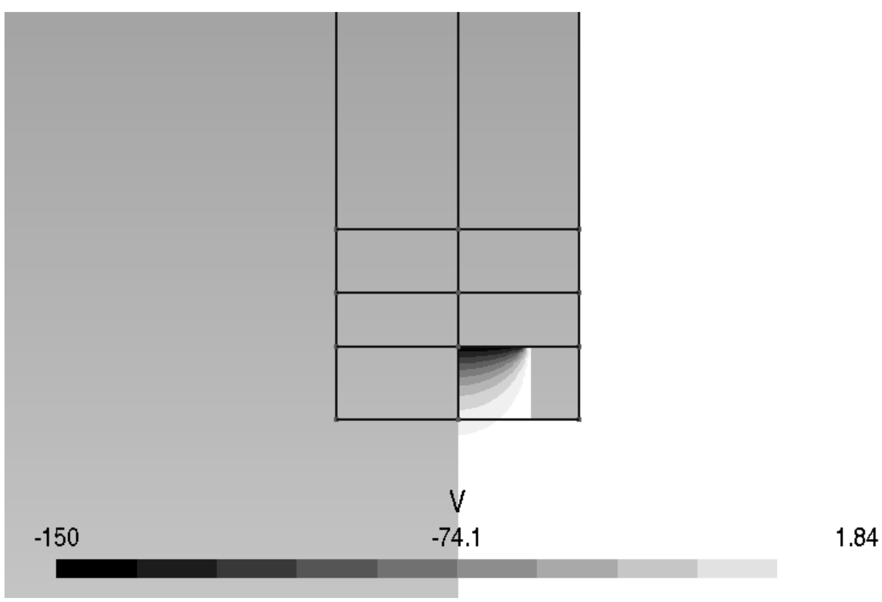

Figure 4.8: Electric potential near probe's front plate, for $N = 1 \cdot 10^{13}$ and $V_{plate} = -150V$.

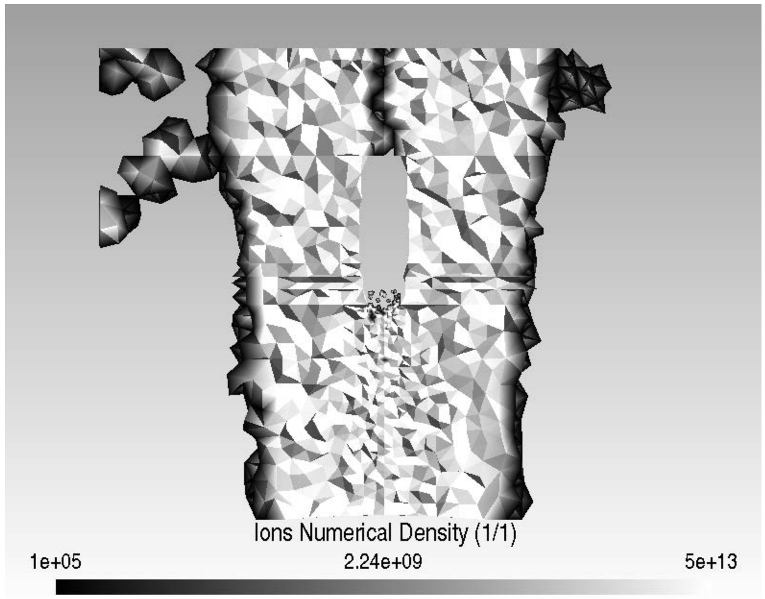

Figure 4.9: Ion density, for $N = 1 \cdot 10^{13}$ and $V_{plate} = -150V$.

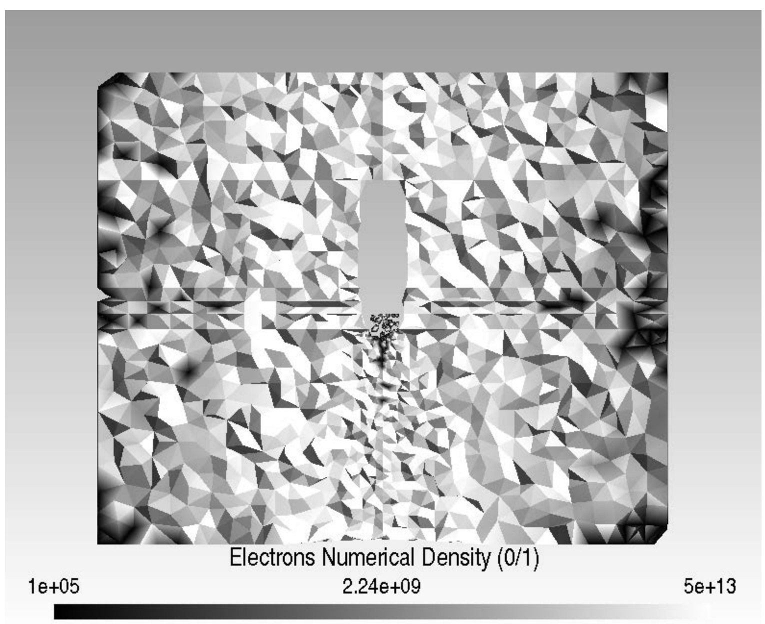

Figure 4.10: Electronic density, for $N = 1 \cdot 10^{13}$ and $V_{plate} = -150V$.

Diagnostic was set on front plate of the probe. Particles at each step that passed trough the collector surface were saved on a text file, letting us calculate current during post-processing. Current measured for the two simulated densities and for all plate potential are shown in graphs in Fig. 4.11 and Fig. 4.12. Ion current remains almost unvaried with probe voltage, while a strong change is visible for electron current at low potential. Saturation curve for measured current is also visible. Ideal ion current is represented by a constant value line. Coefficient C_I and $C_{I,i}$ are finally presented in Fig. 4.13 and Fig. 4.14. One can see how coefficient, at saturation, are almost the same for both densities; the value of coefficient is also in pretty in accordance with one coming from electrostatic model.
PIC results confirm the possibility of improve the probe increasing indent plate distance.
Benefits would be ions current measurement independent from plate potential and plasma density.
Noticing that current increase linearly with density, results appear in line with ions flow measured experimentally. Density given in Tab. 2.1 for plume is an *average* value on section. Density on axis are expected to be higher - up to one order of magnitude.
Experimental results, at saturation, gives values for axial ion current around $I_{ions} \approx I = 200\mu A$. Correction coefficient should be considered; we have seen with electrostatic model that actual probe suffers focusing more. If we assume that coefficient C_I found with electrostatic model to be right, then $I_{ions,undisturbed} = \frac{I_{measured}}{C_I} = \frac{200\mu A}{1.316} = 1.520\mu A$. Comparing with results of simulation, a density of $N \approx 9 \cdot 10^{15} m^{-3}$ is expected in region of probe.
A similar value for expected density may be found using experimental result with the same correction coefficient, but using definition of current and assuming incoming velocity to be known, so $I_{ions,undisturbed} = evN\pi r^2_{ions,undisturbed} = evN\pi r^2_{plate}$; one obtains $N = 6.7 \cdot 10^{15} m^{-3}$.
Exact value of density on the axis, in the section of measurement, is not currently verifiable.

So far, the most important result obtained with PIC model is agreement with electrostatic model. One can develop electrostatic model to obtain a good description of probe performances.

Improvements for new models

Improvements on model used for this simulation should take into account magnetic field, and verify results on more densities. Moreover, undisturbed flow should be calculated using a different geometry respect probe's one, solving plasma equation also inside that domain. Bigger domains, in a way compatible with computational capabilities and time, may be developed.
Finally, a model should be developed with entire thruster to evaluate possible coupled effects.

4.5 Secondary emission

Secondary emission in is a phenomenon where primary incident particles of sufficient energy, when hitting a surface or passing through some material, induce the emission of secondary particles. Secondary emission for Argon ions hitting a metal surface can be quantified

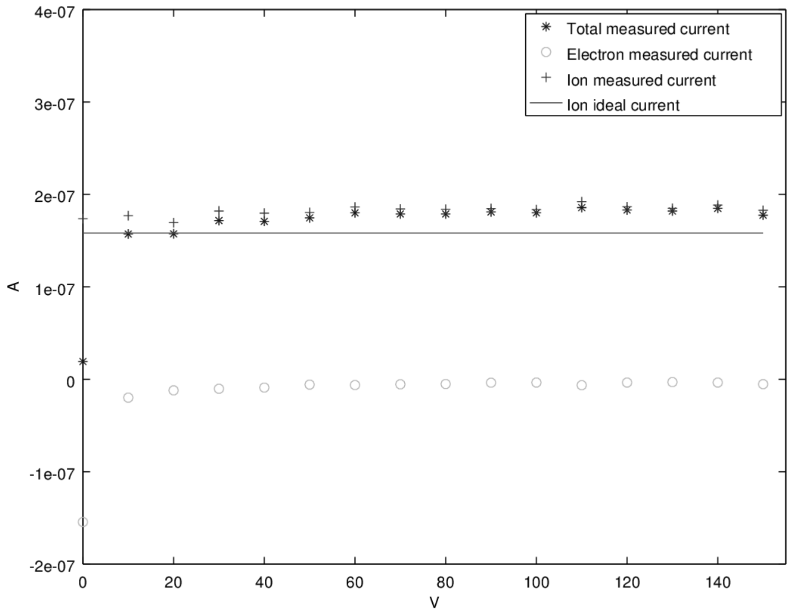

Figure 4.11: Current passing through probe's front plate for $N = 1 \cdot 10^{13}$.

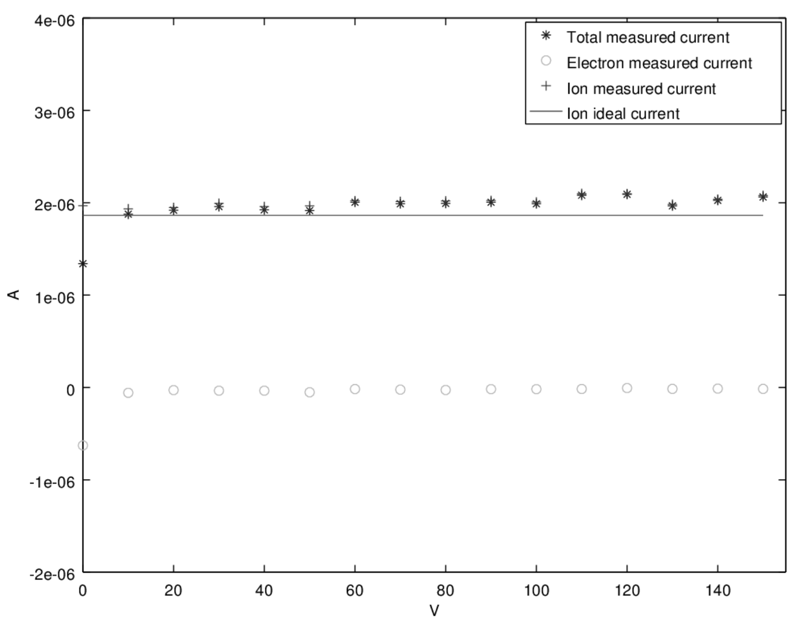

Figure 4.12: Current passing through probe's front plate for $N = 1 \cdot 10^{14}$.

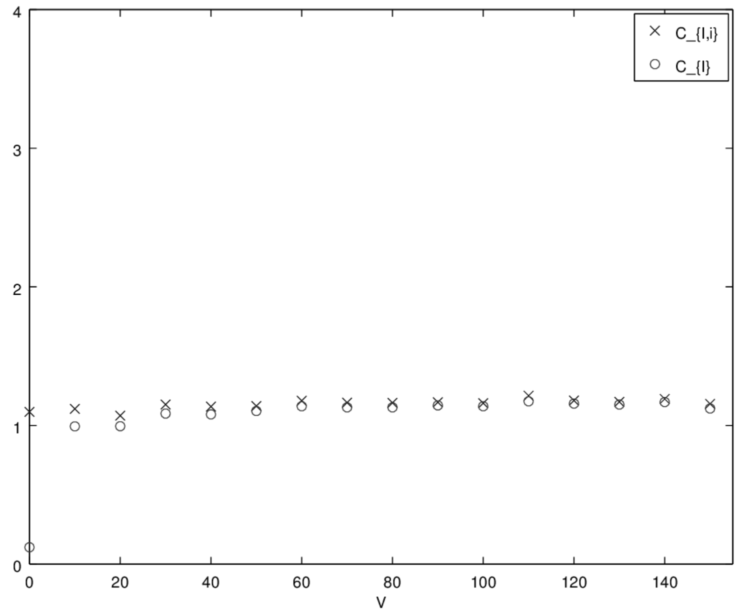

Figure 4.13: Correction coefficient for $N = 1 \cdot 10^{13}$.

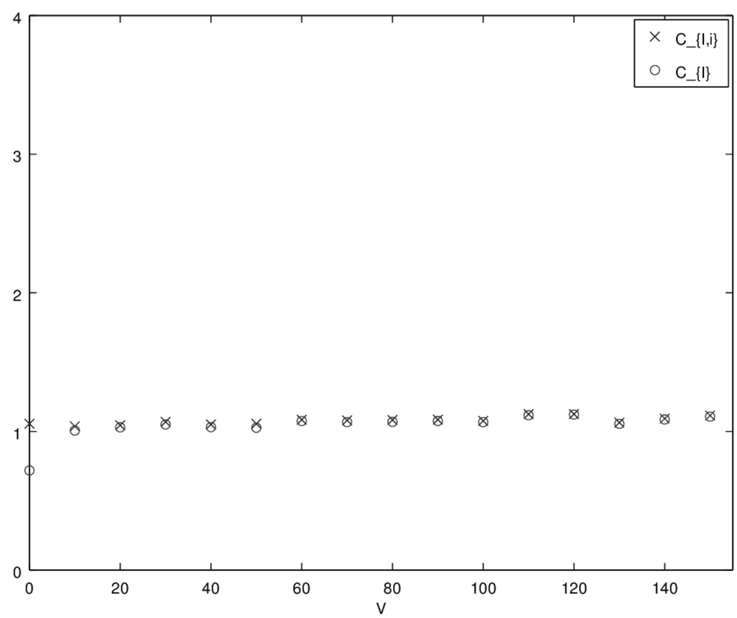

Figure 4.14: Correction coefficient for $N = 1 \cdot 10^{14}$.

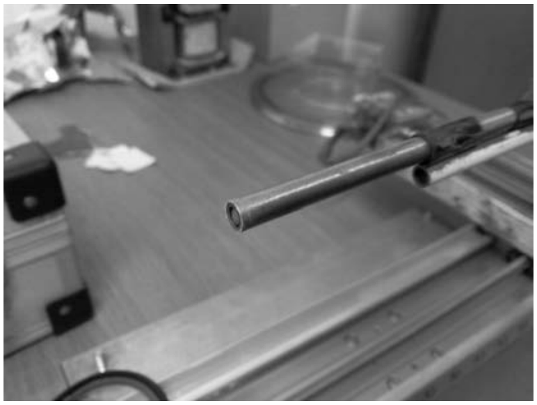

(a)

(b)

Figure 4.15: Faraday probe before (a) and after (b) modification.

using a coefficient γ present in literature [3, 22, 29]. Although the secondary electron emission depends on the surface conditions and on the energy of the impacting ions, in practical applications, the coefficient γ is often considered as a constant leading to a serious disagreement between experimental and simulation results. If we considered the energy dependence of the electron yield per ion in accordance with [3], two different coefficients are given. One is for atomically clean surface, while the other for dirty surfaces; they are both based on a large set of experimental data for discharges in Argon and various electrode materials (Cu, Au, Pt, Ta).
One for dirty surfaces is

$$\gamma = \frac{m_{electrons,emitted}}{m_{ions,incident}} = \begin{cases} \frac{0.006E_i}{1+\left(\frac{E_i}{10}\right)^{1.5}} + 1.05 \cdot 10^{-4} \frac{(E_i-80)^{1.2}}{1+\frac{E_i}{8000}^{1.5}} & E_i > 80eV \\ \frac{0.006E_i}{1+\left(\frac{E_i}{10}\right)^{1.5}} & E_i \leq 80eV \end{cases} \tag{4.8}$$

with E_i energy of ions expressed in eV, and may be used to keep into account secondary emission in PIC simulation data; γ increases with incoming ion beam energy.
In our case, ion energy increases with plate potential, from a value of $\frac{1}{2}m_i v_{undisturbed}^2 \approx 80eV$ to a value of $230eV$. As one can understand, current will be overestimated and will increase more with ions energy - with plate voltage. With formulation above one can find that secondary effect may affect results up to a 5%.
Results obtained in our model may be modified to account for this correction.

4.6 Experimental measurements and results comparison

Eventually, an experimental validation of previous results was tried. Experiments where done at CISAS laboratories. A Faraday probe - with a small indent - was modified as illustrated in Fig. 4.15; a ground ring was added in front of the probe to simulate improved probe and enhance potential drop.
Current was measured with modified Faraday probe at different plate voltages for two different distances of the probe from outlet section. This aimed to verify independence of

V_{plate}, $[V]$	I_{105mm}, $[\mu A]$	I_{155mm}, $[\mu A]$
0	33	19
−8.9	50	21
−17.8	60	24
−26.6	64	26
−35.5	68	27
−44.5	73	29
−52.6	76	30
−60.8	80	32
−69	83	32.6
−77.2	86	33.7
−86.1	89	34.5
−94.3	92	35.2
−98.2	94	35.7
−106.4	96	36.2
−114.6	99	36.9
−120.8	100	37
−128.6	103	37.7
−136.8	105	38.2
−145	107	39
−151.3	108	39.5
−159.2	109	40
−167.3	110	40.6

Table 4.7: Values for current measured with modified Faraday probe during experimentation at two different distances from outlet section.

saturation curve from density. As axial distance increases, density decreases to conserve flux of particles in a diverging flow. Distances for measurements are $105mm$ and $155mm$. Measurements were taken for an Argon flow mass flow of $\dot{m} = 0.125\frac{mg}{s}$, an operation frequency of $7.58MHz$ and a power of $50W$. These $I_{measured} - V_{plate}$ are compared in Fig. 4.16 to those collected in same operational condition but a inflow rate of $\dot{m} = 1.15\frac{mg}{s}$ with probe before modification, already present at CISAS, and with ones from simulations in Fig. 4.11-4.12.
Results are given in Tab. 4.7.
$I_{measured} - V_{plate}$ curves are expected to be scalable at saturation; at low voltages results may differ because of different potential of plasma. Comparisons must be done at voltages high enough to make plasma potential differences negligible respect to plate potential (say $\approx 30V$).
Post-processed curves shows a behaviour that must be further investigated. Invariance with density, that may be considered verified from simulations, is not confirmed from experimental curves; moreover, the curve differs sensibly - there's no invariance with V_{plate} in laboratory ones. Experimentation results show smoother saturation curves, while computed ones reach suddenly maximum value.
A so strong error can not be connected only to secondary emission. Moreover, these curves

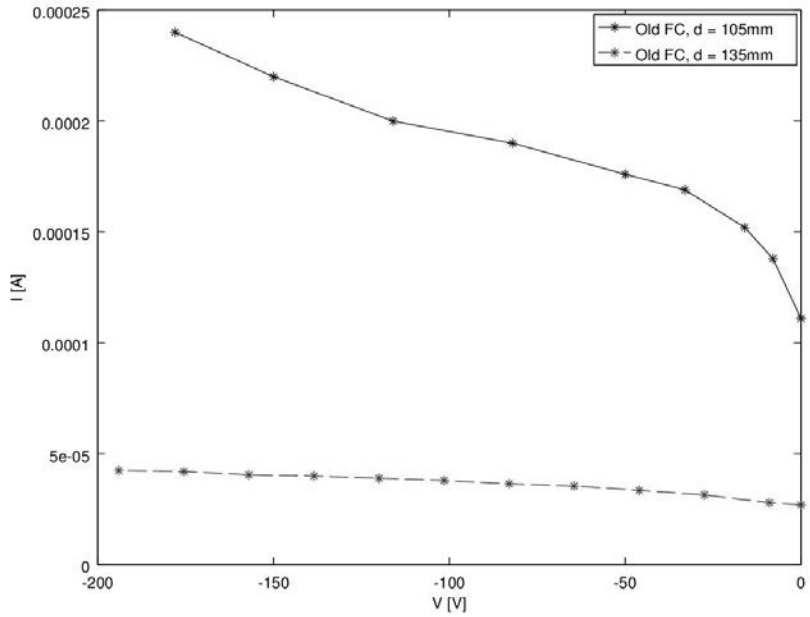

(a)

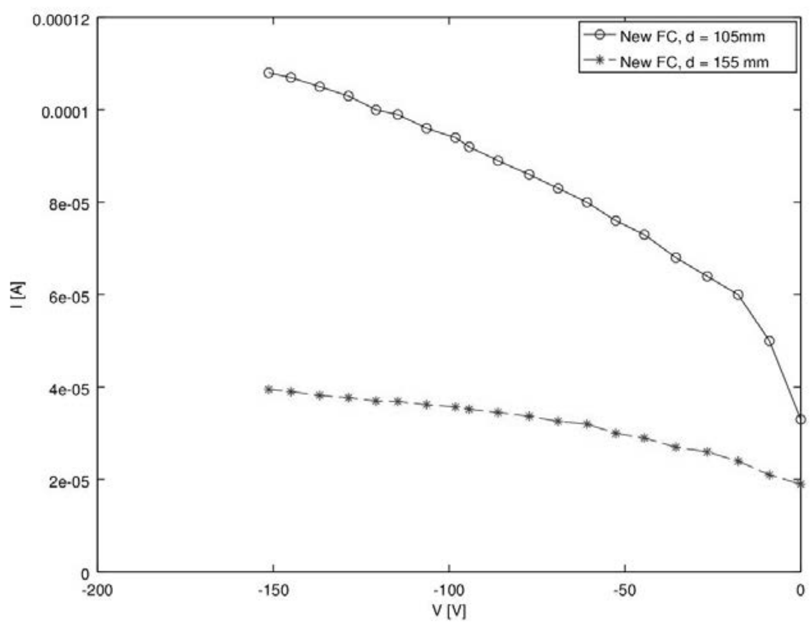

(b)

Figure 4.16: Results before (a) and after (b) modification.

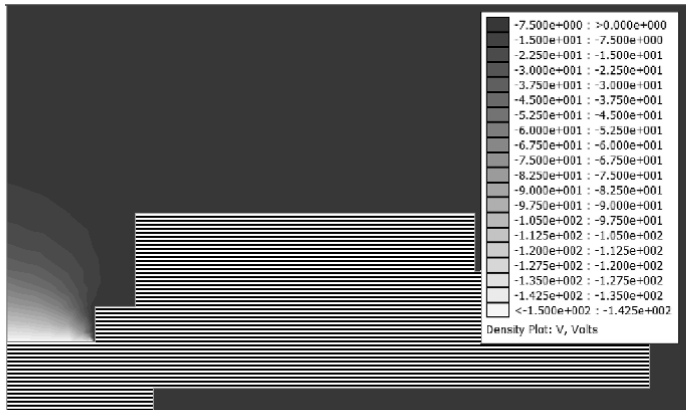

Figure 4.17: Electric potential solution on front of the real FC.

are close to original ones.
Such results should be not interpreted as a failure of design criteria. An insight on experiment lead us to say that it did not represent theoretical conditions. Modification of the experiment, because of practical realisation in laboratory time and possibilities restraints, did not give an accurate representation of probe modeled during numerical analysis. Some rings were used to increase indent of FC front plate, but internal diameter differed from sensor diameter.
A FEM solution for probe front face after modification, once investigated, is represented in Fig. 4.17.
One can see how potential drop expand radially inside the ring hole, leading to focusing effect - and then to dependence on plate voltage and density.
Never mind, we can use results to validate electrostatic model using FEM solution for experimental conditions and a iterative code integrating particle trajectories as explained in 4.2 and 4.3. We also take into account γ correction due to secondary emission, correcting the ion current; final correction coefficient is found as

$$C_I = \frac{I_{measured}}{I_{ions,undisturbed}} \approx \frac{I_{ions,measured}}{I_{ions,undisturbed}} = C_{I,i}|_{FEM} \cdot (1 + \gamma) \tag{4.9}$$

and holds for saturation region. Values for $C_{I,i}|_{FEM}$, γ and C_I are given in Tab. 4.8 and finally the experimental curve is plotted with one corrected for saturation region ($V_{plate} > 30V$) in Fig. 4.18.
Correction gives an almost horizontal curve, as we expect. Deviation from perfect horizontality may be connected to:

- approximation of electrostatic model;
- approximations in secondary emission coefficient;
- uncertainties in incoming plasma temperature and speed;
- fast electrons;

V_{plate} $[V]$	$C_{I,i}\|_{FEM}$	γ	C_I
0	1	0.020410	1.0204
10	1.0268	0.021344	1.0487
20	1.0404	0.022742	1.0641
30	1.054	0.024447	1.0798
40	1.0816	0.026388	1.1101
50	1.0955	0.028521	1.1267
60	1.1095	0.030815	1.1437
70	1.1378	0.033248	1.1756
80	1.152	0.035804	1.1932
90	1.1664	0.038467	1.2113
100	1.1808	0.041228	1.2295
110	1.1954	0.044076	1.2481
120	1.2247	0.047003	1.2823
130	1.2395	0.050004	1.3015
140	1.2544	0.053073	1.3210
150	1.2694	0.056204	1.3407

Table 4.8: Values of correction coefficients for modified probe.

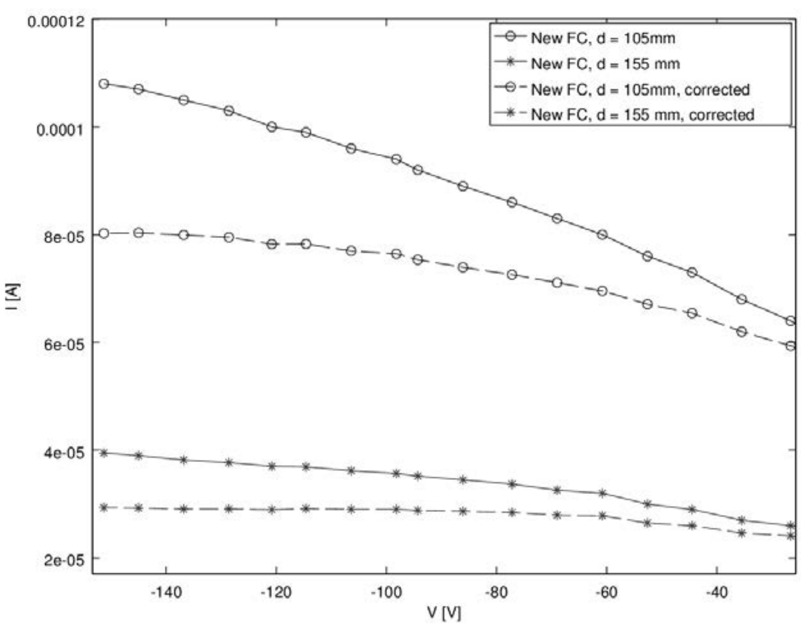

Figure 4.18: Experimental $I-V$ curves obtained with modified FC after correction.

- thermalization of the motor during the experiment.

As a reference, same coefficient calculated with a 10% slower velocity is given in appendix; variation on C_I goes up to a 6%. Anyway, an uncertainty around 20% can be considered satisfactory.
If we apply the same method for actual faraday probe using results from 4.2 and calculating γ from 4.8, we may correct results from first measurements (Fig. 4.16 (a)). Results are presented in 4.9 and Fig. 4.19.
Values of current between the two measurements at same distance differs probably for differences on inflow rate, that influence ionization efficiency and flow evolution; furthermore, thermalization of the motor deeply modify values of current during time. Anyway, the important result is that curves are almost horizontal, giving us a value for ion current in that specific case.

4.6.1 Future experiment

An experimentation is expected to verify prevision with theoretical model to realize a V_{plate} and density independent probe. Care must given, during realization of experimental model, to accurately respect indent and internal radius dimensions.

V_{plate} $[V]$	$C_{I,i}\vert_{FEM}$	γ	C_I
0	1	0.02041	1.0204
10	1.0228	0.021344	1.0446
20	1.0445	0.022742	1.0683
30	1.0664	0.024447	1.0925
40	1.0885	0.026388	1.1172
50	1.1095	0.028521	1.1411
60	1.1307	0.030815	1.1655
70	1.1506	0.033248	1.1889
80	1.1722	0.035804	1.2142
90	1.191	0.038467	1.2368
100	1.2129	0.041228	1.2629
110	1.2321	0.044076	1.2864
120	1.2514	0.047003	1.3102
130	1.2709	0.050004	1.3345
140	1.2905	0.053073	1.359
150	1.3103	0.056204	1.3839

Table 4.9: Values of correction coefficients for original probe.

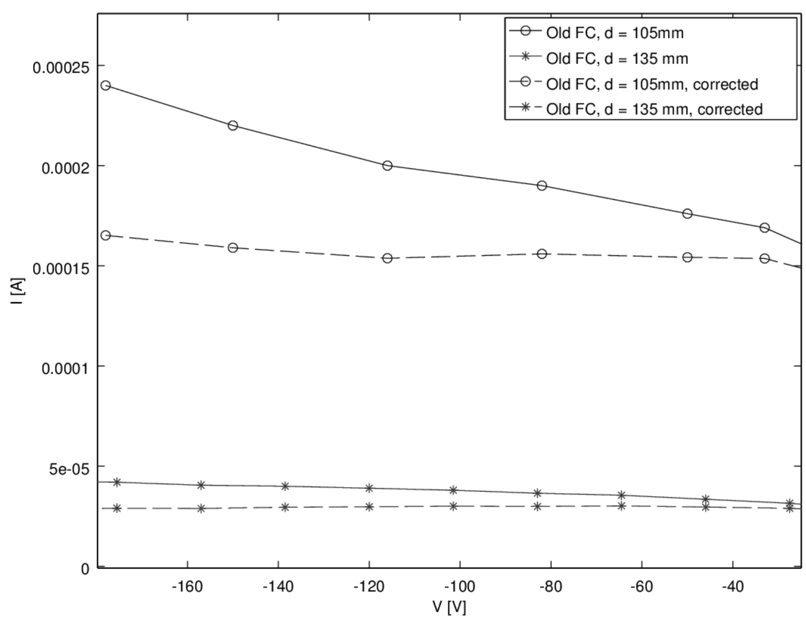

Figure 4.19: Experimental $I - V$ curves obtained with original FC after correction.

Chapter 5

Conclusions

The work aimed to find effect of new components on actual thruster performances and to define a correction coefficient to account for focusing effect on ion current measurement with a Faraday probe at the plume. Both arguments were investigated using electrostatic FEM models or PIC software. Results were compared with experimental evidences already present at CISAS; a new experiment was tried for validation of an improved Faraday cup.

About influence of components, only some of them give a net increase on performances, while other lead to worsening or instabilities. Results show that:

- capacitor at the outlet section in addition to a convergent magnetic field gives better performances; its positive effect comes from the pulsating behaviour it gives to the thruster. Electrons are accelerated for a semi-period, and with them all plasma flow thanks to ambipolar diffusion; moreover, in this lapse of time mass flow is higher than average one. In the other semi-period, electrons are decelerated leading to slower plasma: flow rate is also lower. Averaging on a period, capacitor has a globally positive effect on thrust and I_{sp};

- external ground ring may be used for enhancing electric field on convergent magnetic field region, amplifying effect described in the previous point;

- internal cylinders inserted in the chamber lead to instabilities that are probably connected to azimuthal currents; neutral fluid-dynamics effect should be further investigated;

- physical nozzle may be used to control alignment of electric and magnetic field using its dielectric and diamagnetic coefficients. The effect does not seem to have a strong impact on axis zone;

- external rings at the same potential as the inner capacitor plate, that may be used to collimate flow, have a negative effect on total thrust and I_{sp}. Effect of finite phase shifts between capacitor voltage and external rings voltage should be further investigated.

Eventually, evaluation of ion convergence on Faraday cup shows that focusing effect in actual condition is present and not negligible. A correction coefficient may be defined for this configuration, but it would be variable with plate potential and plasma density. A modification of the probe can lead to a measuring instrument almost uninfluenced by these quantities. More in detail:

- focusing effect increase with front probe's plate potential and decrease with density due to shielding effect;
- focusing effect may be corrected efficiently with electrostatic model. This model gives good results at low focusing effect regime;
- plate potential and plasma density influence measurements when ion convergence to the plate is high;
- improvements on actual probe may be achieved increasing plate indent respect to front section; that leads to a reduction of the influence of plate potential and plasma density;
- electrostatic and PIC models give same result for the improved probe;
- improvements on Faraday cup should be experimentally proven.

Appendix A

Further results

Some additional results that may be of interest are given below. They are not inserted in the main body to keep it slim and fluent.

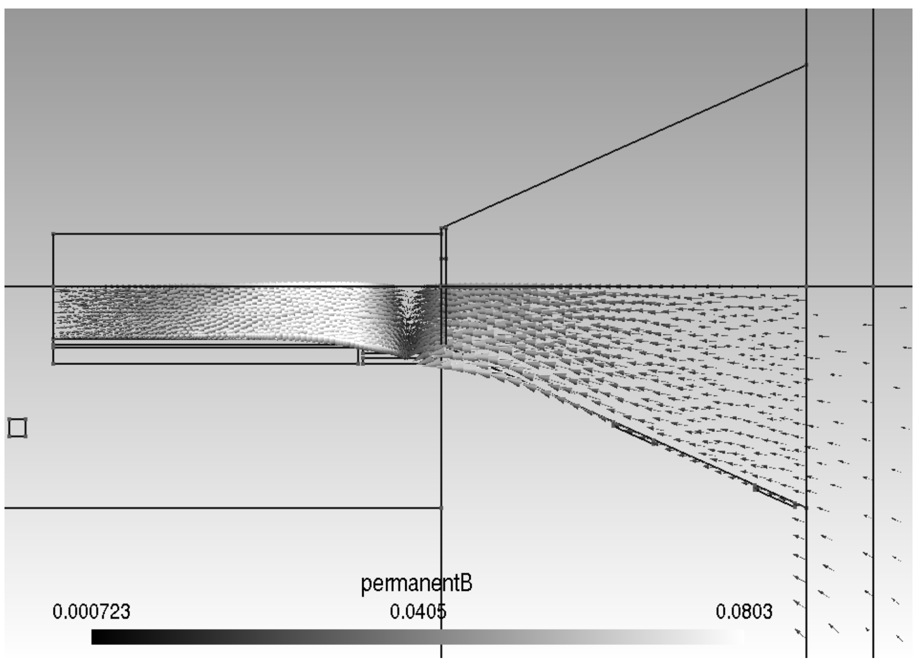

Figure A.1: Magnetic field for all PIC simulations.

A.1 Effect of the capacitor

Effect of the capacitor may be evaluated with the same PIC model developed for the external rings at same potential of the capacitor.
The only modification needed to use the model was to exclude the capacitor and all external rings from the boundary conditions for the field solver.
Results obtained from this simulations are given below.

	T_{max} $[N]$	$I_{sp,max}$ $[s]$	I_{tot} $[Ns]$	T $[N]$	I_{sp} $[s]$
No capacitor	$1.1685 \cdot 10^{-7}$	$58235 \cdot 10^{4}$	$1.4140 \cdot 10^{-13}$	$2.829 \cdot 10^{-8}$	2218

Table A.1: Complete thruster results without capacitor. Total impulse is computed for $\Delta t = 5 \cdot 10^{-6} s$.

Computational limitations allow a maximum density much lower than real one in the chamber. In numerical simulation conditions, antenna potential is enough to give a pulsating behaviour to the thruster. In actual conditions, high density on the chamber means that quasi neutrality is respected in almost all the chamber. Then real effect of antenna is expected to be, in real conditions, less influential; the thruster than presents almost steady state constant performances. Nevertheless, benefits on performances using the capacitor are visible also with this model. Results without capacitor are given below; results with capacitor can be found on next section.

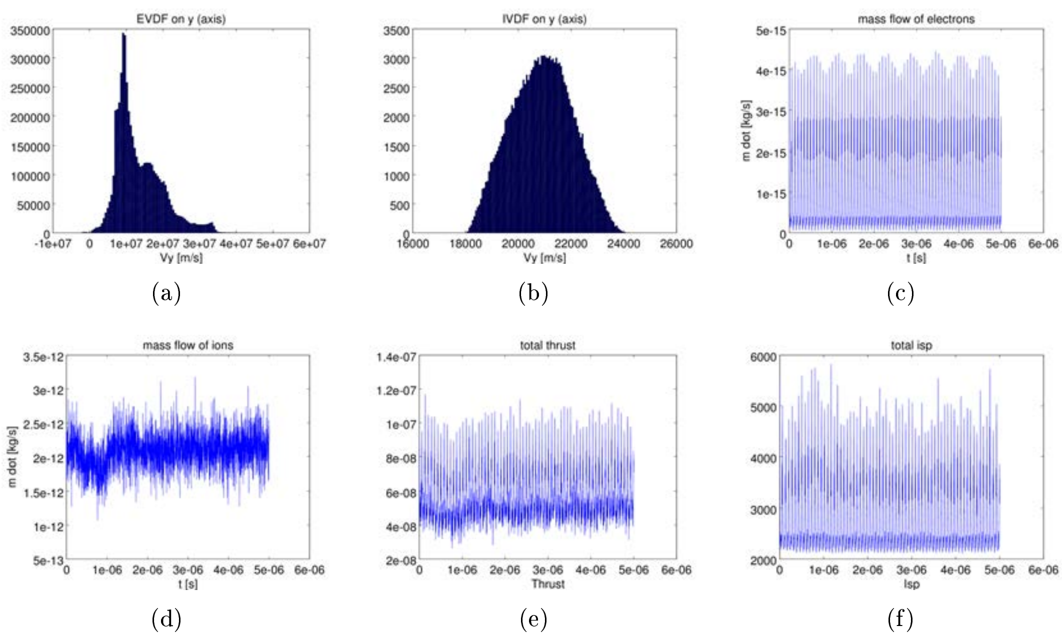

(a) (b) (c)

(d) (e) (f)

Figure A.2: Results from PIC simulation, without capacitor.

A.2 PIC simulation of geometry with external rings

More results for simulations with external rings at the same potential as the capacitor are given.

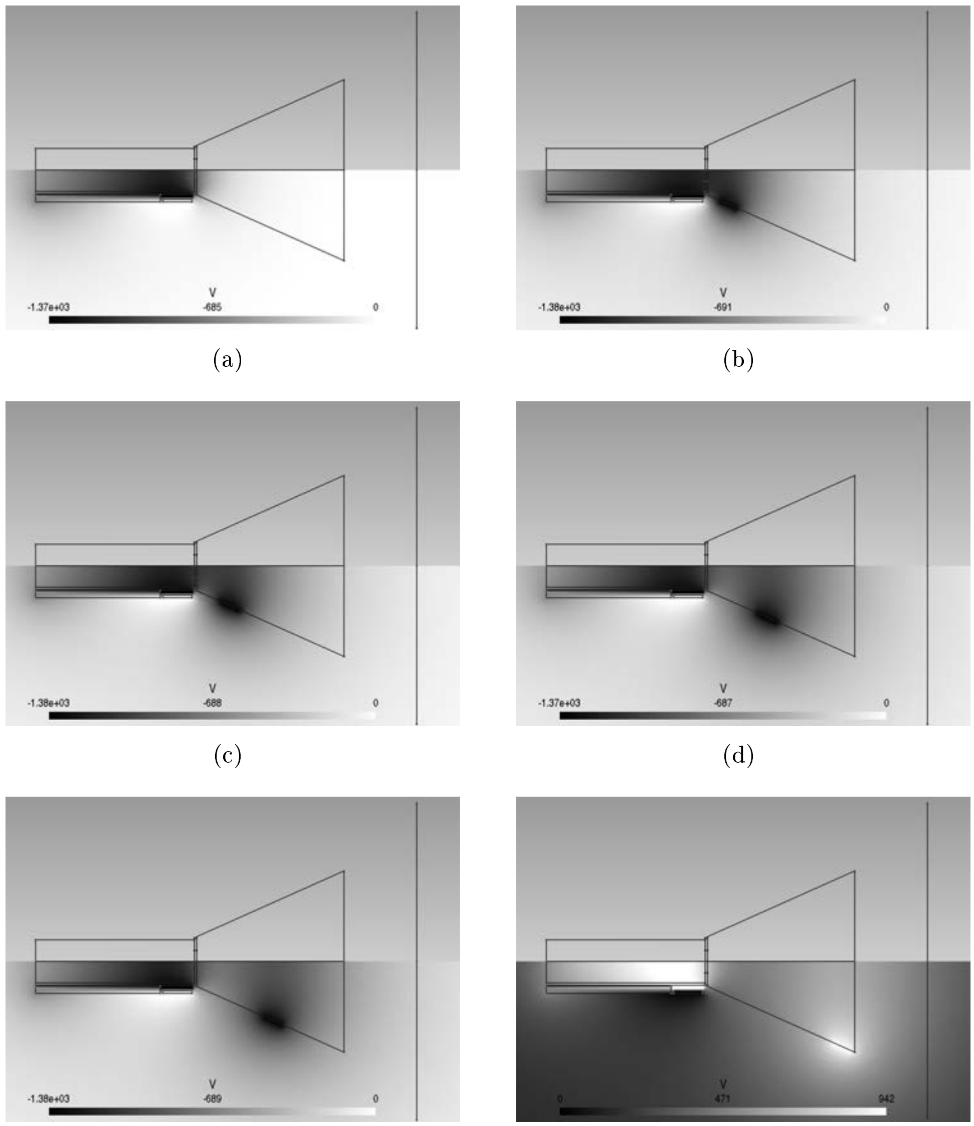

(a) (b)

(c) (d)

(e) (f)

Figure A.3: Electric potential field for all cases, in order from no ring one to E. Last graph is taken at a different time step.

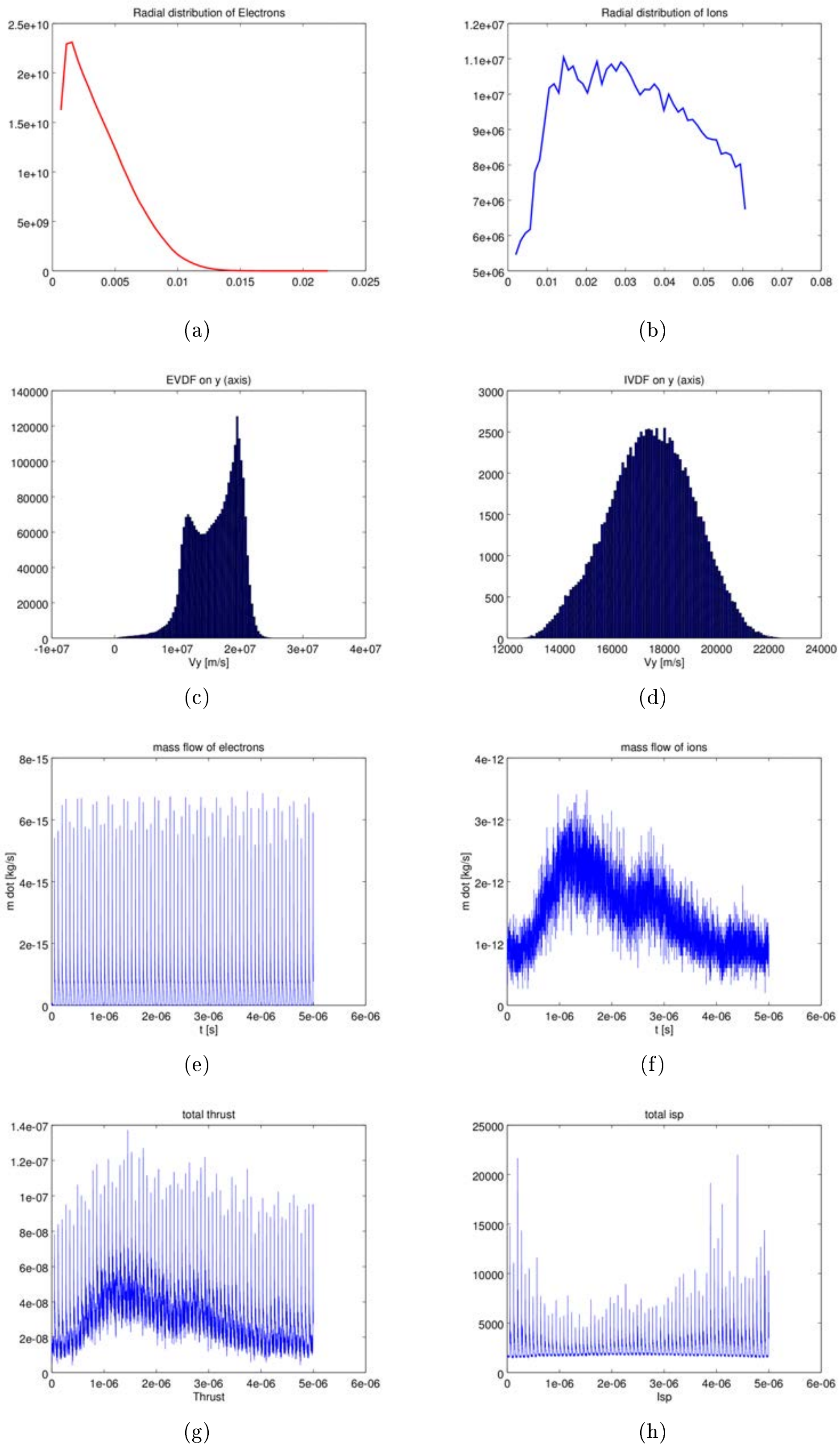

Figure A.4: Results from PIC simulation, without external rings.

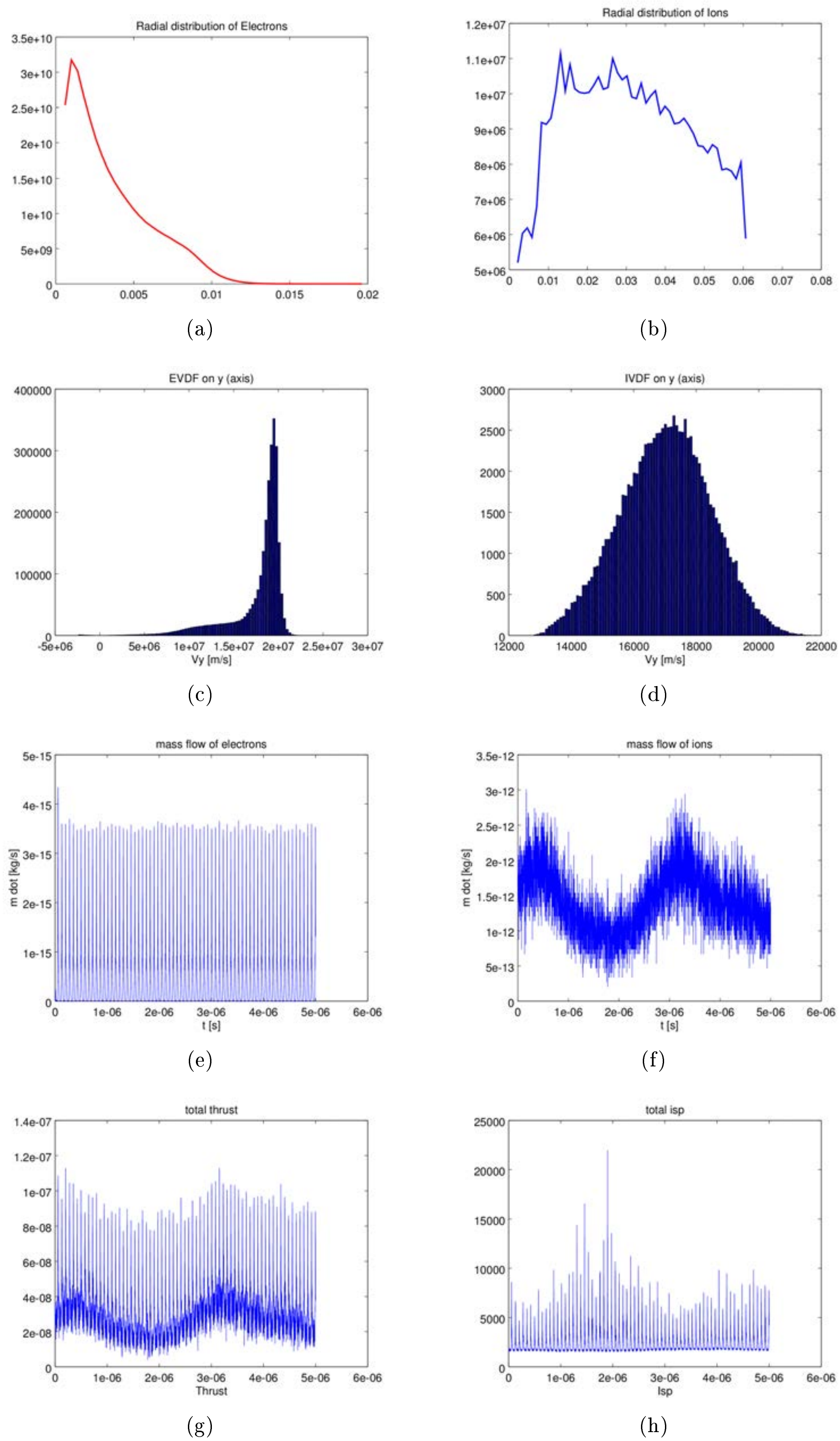

Figure A.5: Results from PIC simulation, case A.

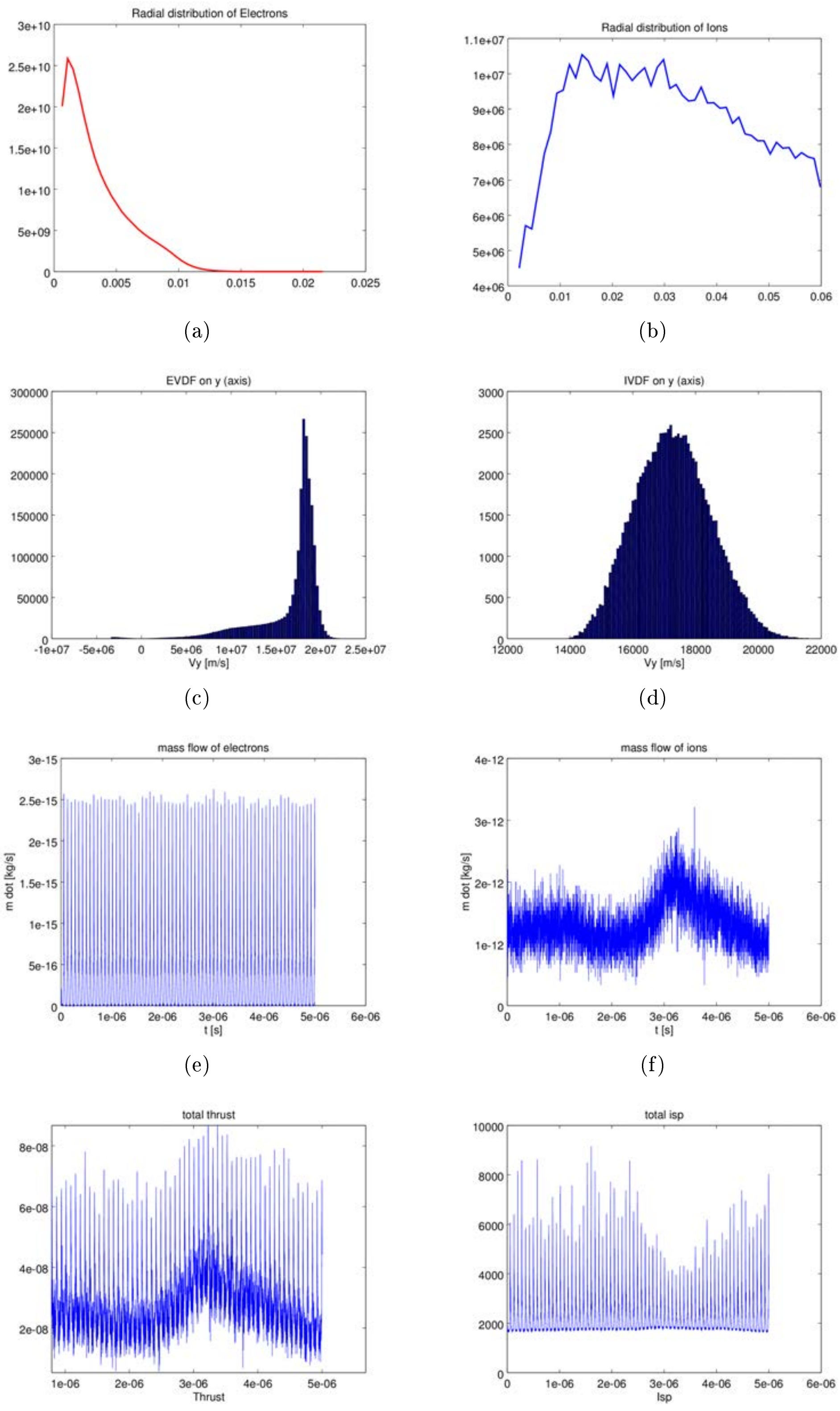

Figure A.6: Results from PIC simulation, case B.

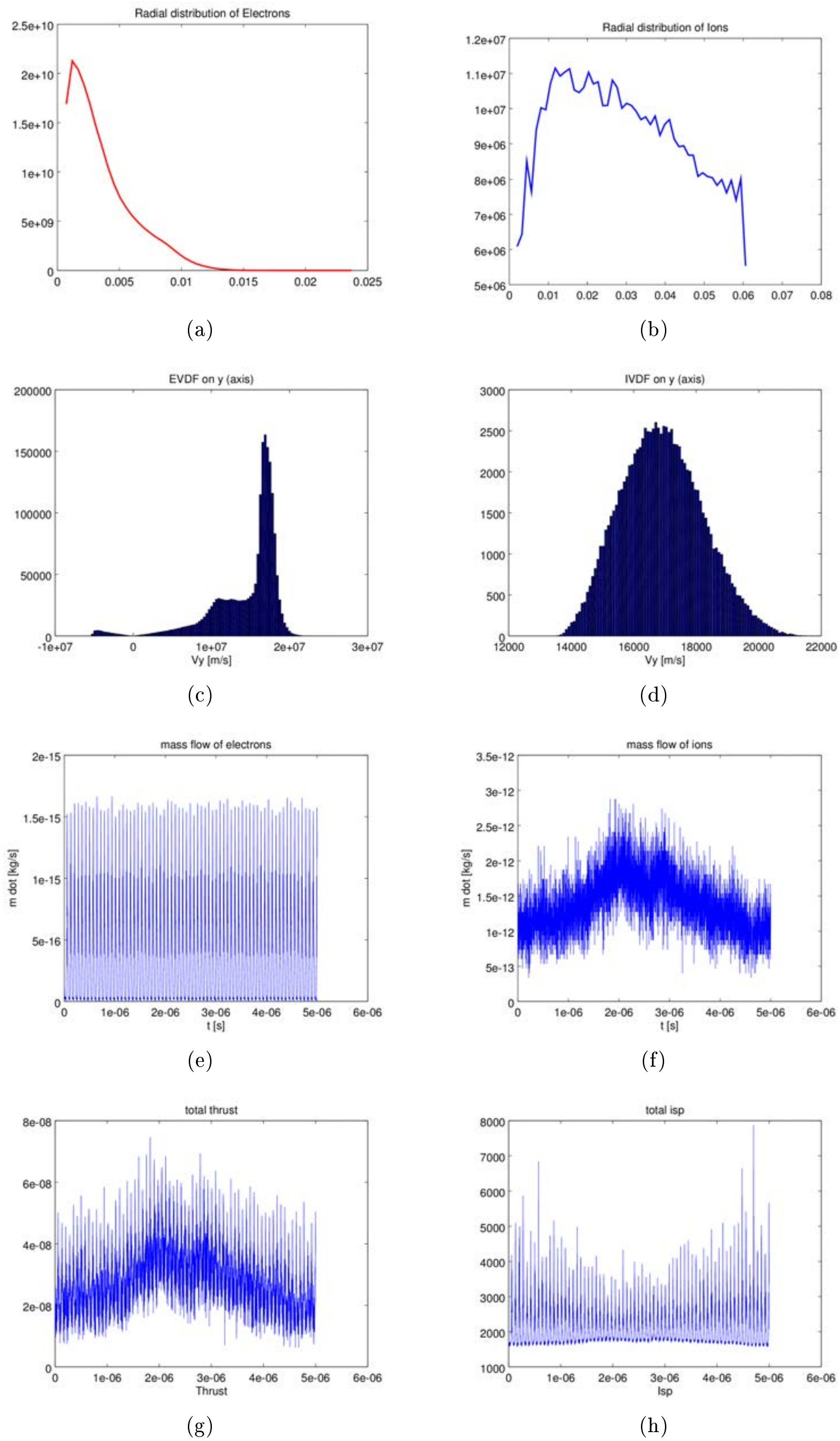

Figure A.7: Results from PIC simulation, case C.

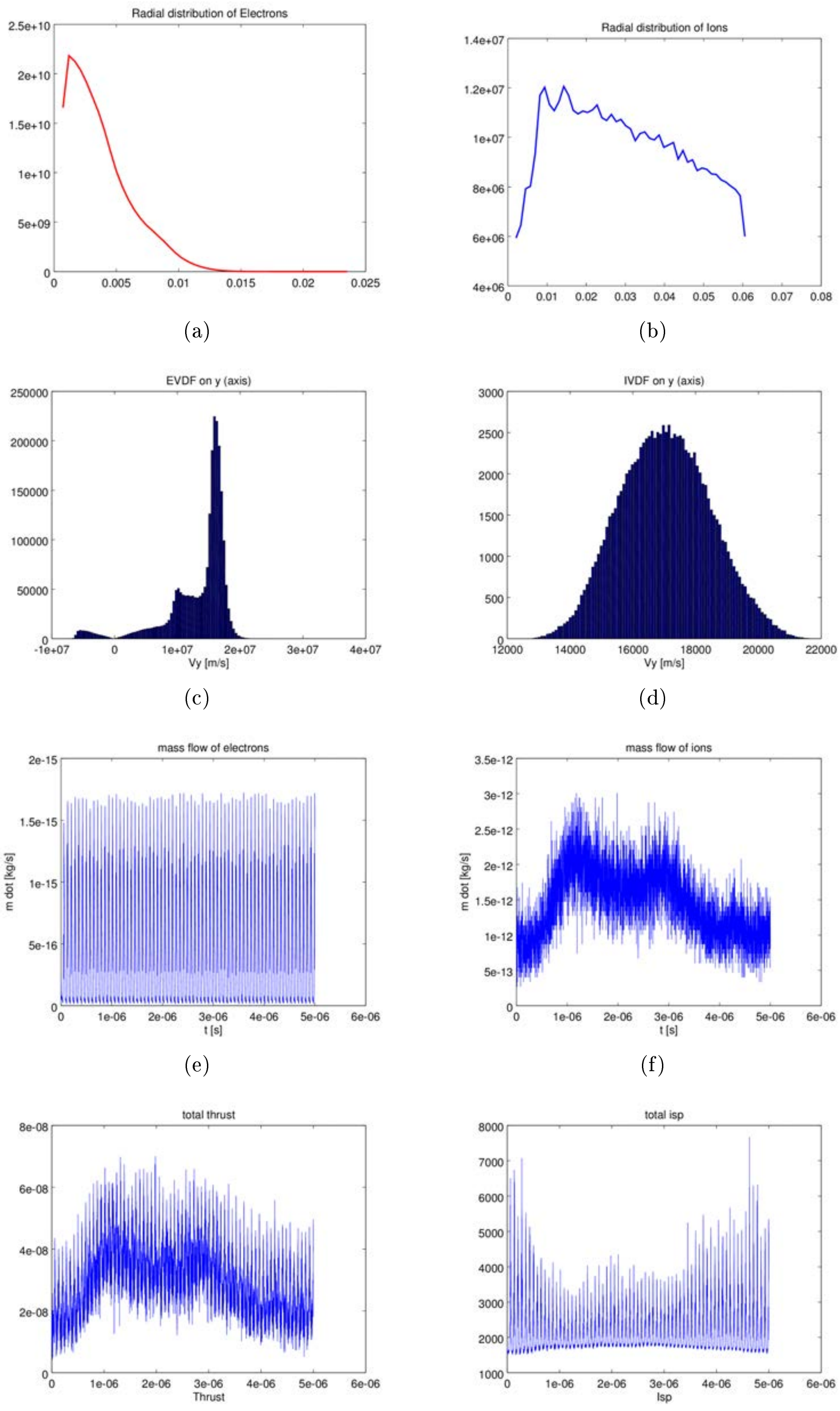

Figure A.8: Results from PIC simulation, case D.

A.3 Electrostatic model for actual Faraday probe

V_{plate} $[V]$	$C_{I,i}\|_{FEM}$	γ	C_I
0	1	0.0218	1.0218
10	1.0282	0.0205	1.0493
20	1.0554	0.0207	1.0772
30	1.0816	0.0218	1.1052
40	1.1081	0.0234	1.1340
50	1.1349	0.0252	1.1635
60	1.1592	0.0272	1.1907
70	1.1852	0.0294	1.2201
80	1.21	0.0318	1.2484
90	1.2335	0.0342	1.2758
100	1.2588	0.0368	1.3053
110	1.2829	0.0395	1.3337
120	1.3072	0.0423	1.3626
130	1.3302	0.0452	1.3904
140	1.3533	0.0482	1.4185
150	1.3767	0.0512	1.4472

Table A.2: Values of correction coefficients for original probe with a 10% incoming slower velocity ($v = 18000m/s$).

A.4 Electrostatic model for improved Faraday probe, PIC simulation of improved Faraday Probe

V_{plate} $[V]$	$C_{I,i}\|_{FEM}$	$C_{I,i}\|_{PIC,1e14}$	$C_{I,i}\|_{PIC,1e13}$	γ
0	1	1.0556	1.0413	0.02041
10	1.0053	1.0375	1.0615	0.021344
20	1.0107	1.045	1.0154	0.022742
30	1.0161	1.0691	1.0913	0.024447
40	1.0201	1.0501	1.0778	0.026388
50	1.0255	1.0553	1.0817	0.028521
60	1.0309	1.0848	1.1172	0.030815
70	1.035	1.0799	1.1047	0.033248
80	1.0404	1.0837	1.1028	0.035804
90	1.0445	1.0857	1.1076	0.038467
100	1.0499	1.0768	1.1009	0.041228
110	1.054	1.1258	1.1518	0.044076
120	1.0595	1.1255	1.1191	0.047003
130	1.0636	1.0636	1.1095	0.050004
140	1.0692	1.0934	1.1297	0.053073
150	1.0733	1.1152	1.0961	0.056204

Table A.3: Values of correction coefficients for improved probe obtained with FEM model and PIC ones; then γ.

Bibliography

[1] Alexey V. Arefiev and Boris N. Breizman. *The Development of the VASIMR Engine.* International Conference on Electromagnetics in Advanced Applications, Torino, Italy, 1999.

[2] Paul M. Bellan. *Fundamentals of Plasma Physics.* Cambridge University Press, 1st edition, 2006.

[3] Aleksandar Bojarov. The influence of the ion induced secondary electron emission on the characteristics of rf plasmas. *Publications of the astronomical observatory of Belgrado*, 2010.

[4] F. F. Chen. *Introduction to Plasma Physics and Controlled Fusion, Vol 1: Plasma Physics.* Springer, 2st edition, 2006.

[5] Francis F. Chen. *Plasma ionization by helicon waves.* Plasma Physics and Controlled Fusion, 1991.

[6] Francis F. Chen. Helicon plasma sources. In *High density Plasma sources*. 1994.

[7] Ira Katz Dan M. Goebel. *Fundamentals of Electric Propulsion: Ion and Hall Thrusters.* John Wiley and Sons, 1st edition, 2008.

[8] John M. Dawson. Particle simulation of plasmas. *Reviews of modern physics*, 1983.

[9] Patrick Dular and Christophe Geuzaine. Getdp 2.4, 2014.

[10] A.V. Arefiev et al. *The Development of the VASIMR Engine.* Institute for Fusion Studies, The University of Texas, Austin, Texas 78712, 1999.

[11] D. Pavarin et al. Design of 50 w helicon plasma thruster. *31st International Electric Propulsion Conference*, 2009.

[12] D. Pavarin et al. Experimental set-up to test a 50w helicon plasma thruster. *31st International Electric Propulsion Conference*, 2009.

[13] D. Pavarin et al. Development of plasma codes for the design of mini-helicon thrusters. *32nd International Electric Propulsion Conference*, 2011.

[14] D. Pavarin et al. Low power rf plasma thruster experimental characterization. *American Institute of Aeronautics and Astronautics*, 2011.

[15] D. Pavarin et al. Thruster development set-up for the helicon plasma hydrazine combined micro research project (hph.com). *32nd International Electric Propulsion Conference*, 2011.

[16] Edgar A Bering III et al. Ambipolar ion acceleration in an expanding magnetic nozzle. *Plasma sources science and technology*, 2011.

[17] Eduardo Ahedo et al. Helicon plasma thrusters: prototypes and advances on modeling. *The 33rd International Electric Propulsion Conference, The George Washington University, USA*, 2013.

[18] Gregor Filipič. Principles of particle in cell simulations.

[19] Christophe Geuzaine and Jean-François Remacle. Gmsh: A 3-d finite element mesh generator with built-in pre- and post-processing facilities. *International Journal for Numerical Methods in Engineering*, 79(11):1309–1331, 2009.

[20] R. W. Hockney and J. W. Eastwood. *Computer Simulations Using Particles*. Adam Hilger, 1988.

[21] Giovanni Lapenta. Particle in cell methods - with application to simulations in space weather.

[22] M.A. Lieberman and A.J. Lichtenberg. *Principles of Plasma Discharges and Materials Processing*. Wiley, 2005.

[23] Max Light and Francis F. Chen. *Helicon wave excitation with helical antennas*. Physics of Plasmas 2, 1995.

[24] David Meeker. Femm: Finite element method magnetics. `http://www.femm.info/wiki/HomePage`. [Online].

[25] David Meeker. Finite element method magnetics: Octavefemm - version 1.2 - user's manual. [Online at `http://www.femm.info/wiki/Documentation`], 2010.

[26] David Meeker. Finite element method magnetics - version 4.2 - user's manual. [Online at `http://www.femm.info/wiki/Documentation`], 2013.

[27] A. Kashefian Naieni, F. Bahrami, N. Yasrebi, and B. Rashidian. Design and study of an enhanced faraday cup detector. *Vacuum*, 83(8):1095 – 1099, 2009.

[28] P.H. Rutherford R. J. Goldston. *Introduction to Plasma Physics*. Taylor and Francis Group, 1st edition, 2000.

[29] E. J. Sternglass. Theory of secondary electron emission by high-speed ions. *Phys. Rev.*, 108:1–12, Oct 1957.

[30] Marek Golkowski Umran S. Inan. *Priciples of Plasma Physics for Engineers and Scientists*. Cambridge University Press, 1st edition, 2010.

[31] Masayuki Yano and Mitchell L. R. Walker. *Plasma ionization by annularly bounded helicon waves*. Physics of Plasmas 13, 2006.